Fuel 321 (2022) 124009

Contents lists available at ScienceDirect

Fuel

journal homepage: www.elsevier.com/locate/fuel

Full Length Article

# Unveiling the deactivation by coke of $NiAl_2O_4$ spinel derived catalysts in the bio-oil steam reforming: Role of individual oxygenates

Leire Landa, Aingeru Remiro, José Valecillos *, Beatriz Valle, Javier Bilbao, Ana G. Gayubo

*Department of Chemical Engineering, University of the Basque Country (UPV/EHU), P.O. Box 644, Bilbao 48080, Spain*

ARTICLE INFO

*Keywords:*
Hydrogen
Steam reforming
Bio-oil
Oxygenates reforming
$NiAl_2O_4$ spinel
Coke deposition
Catalyst deactivation

ABSTRACT

The catalyst stability, mainly affected by coke deposition, remains being a challenge for the development of a sustainable process for hydrogen production by steam reforming (SR) of bio-oil. In this work, the influence of oxygenates composition in bio-oil on the deactivation by coke of a $NiAl_2O_4$ spinel derived catalyst has been approached by studying the SR of a wide range of model oxygenates with different functionalities, including acetic acid, acetone, ethanol, acetaldehyde, acetol, catechol, guaiacol and levoglucosan. A fluidized bed reactor was used in the following conditions: 600 and 700 °C; steam/carbon ratio, 3 (6 for levoglucosan); space–time, 0.034 $g_{catalyst}$ h/$g_{bio\text{-}oil}$ (low enough to favor the rapid catalyst deactivation), and; time on stream, 5 h. The spent catalysts were analyzed with several techniques, including Temperature Programed Oxidation (TPO), X-ray Diffraction (XRD), $N_2$ adsorption–desorption, Scanning and Transmission Electron Microscopy (SEM, TEM) and Raman Spectroscopy. The main factors affecting the catalyst stability are the morphology, structure and location of coke, rather than its content, that depend on the nature of the oxygenate feed. The deposition of pyrolytic and amorphous coke that blocks the Ni sites inhibiting the formation of filamentous carbon causes a rapid deactivation in the guaiacol SR. Conversely, the large amount of carbon nanotubes (CNTs) giving rise to a filamentous coke deposited in the SR of aliphatic oxygenates only causes a slight deactivation. The increase in the temperature significantly reduces coke deposition, but has low impact on deactivation.

## 1. Introduction

Hydrogen is called to play a key role in future energy demand as a substitute for fossil fuels [1]. In fact, in the post-pandemic crisis scenario, the alternatives for the production and use of renewable $H_2$ are taking on great relevance, as for example in the economic recovery package of EU (NextGenerationEU) with €750 billion focused around the European Green Deal, where renewable energy projects highlight, especially wind, solar and kick-starting a clean hydrogen economy, with full economy decarbonization as the target for 2050 [2].

Currently, the most common and economic process for $H_2$ production is the steam reforming (SR) of natural gas, accounting for 76% of the global production, and whose global warming potential per kg of hydrogen produced is 11.956 kg $CO_2$-eq [3]. Although the optimal technology for "green $H_2$" production is the water electrolysis, in the energy transition period until this solution becomes a reality $H_2$ could be obtained with limited $CO_2$ emissions from lignocellulosic biomass, by thermochemical process, particularly gasification, partial oxidation and SR of biomass derivatives (as bioethanol and bio-oil). Some of these processes are currently in a pilot-scale demonstration or at a commercial stage but they require improvements to produce larger competitive volumes [4]. The SR of bio-oil, obtained by fast pyrolysis of lignocellulosic biomass, has gained increased attention [5], due to the good prospects of a strategy to combine the delocalized bio-oil production (with well-developed technologies and with low infrastructure costs) [6], with centralized bio-oil SR in a bio-refinery with units designed ad hoc for selective $H_2$ production. The liquid state and higher volumetric energy density of bio-oil facilitates its transportation, storage and treatment compared to biomass [7]. In addition, the SR of bio-oil avoids the costly dehydration steps required for the use of bio-oil as fuel or for its valorization in other catalytic processes [8].

Bio-oil is composed of an oxygenate mixture with the presence of different functional groups (carboxyl, ester, carbonyl, ether, phenolic and hydroxyl groups) and variable water content (depending on the origin of the biomass). The SR reaction of oxygenated hydrocarbons ($C_nH_mO_k$) to produce syngas ($H_2$ + CO) can be described by the following equation:

* Corresponding author.
*E-mail address:* jose.valecillos@ehu.eus (J. Valecillos).

https://doi.org/10.1016/j.fuel.2022.124009
Received 24 February 2022; Received in revised form 23 March 2022; Accepted 25 March 2022
Available online 18 April 2022

$$C_nH_mO_k \ + \ (n-k)H_2O \rightarrow nCO \ + \ (n+\frac{m}{2}-k)H_2 \quad (1)$$

In addition to the main reaction (Eq. (1)), the water gas shift (WGS) reaction (Eq. (2)) takes place, and thus the overall SR equation for the oxygenates is defined by Eq. (3).

$$CO \ + \ H_2O \leftrightarrow \ CO_2 \ + \ H_2 \quad (2)$$

$$C_nH_mO_k \ + \ (2n-k)H_2O \rightarrow nCO_2 \ + \ (2n+\frac{m}{2}-k)H_2 \quad (3)$$

$H_2$ yield is also affected by reactions occurring in parallel to oxygenates SR and WGS reactions, such as decomposition/cracking (Eq. (4)), which affects the catalyst stability due to coke deposition, SR of decomposition products ($CH_4$ and hydrocarbons, (Eqs. (5) and (6)), and interconversion of oxygenates (Eq. (7)).

$$C_nH_mO_k \rightarrow C_xH_yO_z \ + \ gas \ (CO, \ CH_4, \ CO_2, \ C_aH_b, \ H_2, \ \ldots) + coke \quad (4)$$

$$CH_4 + \ H_2O \leftrightarrow \ CO \ + \ 3H_2 \quad (5)$$

$$C_aH_b \ + \ aH_2O \rightarrow aCO \ + (a \ + b/2)H_2 \quad (6)$$

$$C_nH_mO_k \rightarrow C_xH_yO_z \quad (7)$$

Moreover, the reactions for coke formation from gaseous products (Eqs. (8) and (9)) and its gasification reaction (Eq. (10)) should be considered, as they may affect catalyst stability and also the products yields when they are highly promoted.

*Hydrocarbon decomposition*: $C_aH_b \rightarrow (b/2)H_2 + aC$ (8)

*Boudouard reaction*: $2CO \leftrightarrow C + CO_2$ (9)

*Coke gasification*: $Coke + H_2O \rightarrow CO + H2$ (10)

One of the main problems or bottlenecks of bio-oil SR is the rapid deactivation of the catalyst, which justifies that it receives a great attention, in order to prepare stable catalysts. Deactivation studies have generally been carried out with model oxygenates [9–20], with mixtures of oxygenates [21–23], and studies with raw bio-oil are limited. [24–29]. The results show the importance of the nature and location of the coke in the deactivation of the catalyst. Thus, the formation of carbon filaments has a reduced incidence in the deactivation, whose responsibility falls mainly on the formation of amorphous coke encapsulating the Ni sites. There is also a general tendency to relate the formation of deactivating amorphous coke to the SR of some families of oxygenates (phenols, carboxylic acids, furfural and saccharides, mainly).

This paper delves into the clarification of deactivation by coke of a catalyst derived from $NiAl_2O_4$ spinel, which has been previously proven to have high activity and selectivity to $H_2$ in the reforming of raw bio-oil and, more interestingly, it can be fully regenerated by coke combustion at 850 °C (with spinel reconstruction) [30]. For that purpose, we have studied the influence on the deactivation behavior and coke deposition of individual oxygenate compounds with varied functional groups present in bio-oil (acetic acid, acetaldehyde, acetol, ethanol, acetone, catechol, guaiacol and levoglucosan). The evolution along time on stream of the conversion and products yields in the SR of each individual compound have been analysed, as well as the amount, nature, morphology and location of the coke deposited on the catalyst used by means of several techniques: temperature programed oxidation (TPO), X-ray diffraction (XRD), $N_2$ adsorption–desorption, scanning and transmission electron microscopy (SEM, TEM) and Raman spectroscopy. The experimental conditions used are similar to those previously used in the SR of raw bio-oil with the same catalyst [31], which has allowed a direct comparison of the catalyst performance in the SR of each individual oxygenate with that obtained in the SR of raw bio-oil. The results have allowed stablishing the main responsible of catalyst deactivation during SR of bio-oil, as well as the coke characteristics that mainly affect the deactivation of the catalyst. Consequently, interesting information is obtained to adjust the composition of the raw bio-oil in order to attenuate catalyst deactivation by coke. In addition, the oxygenates of greatest interest as model compounds for the comparison tests of catalyst deactivation for the SR of raw bio-oil are identified.

## 2. Experimental

### 2.1. Pure oxygenate compounds

The pure oxygenate compounds selected as representative of the major families of oxygenates in bio-oil are the following: acetic acid (AA) (Romil LTD, purity > 99.9 %), acetaldehyde (AD) (Merck KGaA, purity ≥ 99 %), acetone (A) (AppliChem GmbH, purity ≥ 99.9 %), acetol (AT) (hydroxyacetone, Alfa Aesar GmbH, purity = 95 %), ethanol (E) (Merck KGaA, purity ≥ 99.9 %), 1,2-benzenediol or catechol (C) (Sigma-Aldrich, purity ≥ 99 %), levoglucosan (L) (1,6-Anhydro-β-D-glucopyranose, Acros Organics, purity > 99%), and 2-methoxyphenol or guaiacol (Alfa Aesar GmbH & Co, purity > 98 %) dissolved in 50 wt% of ethanol (G + E) due to its low solubility in water. Acetone, acetaldehyde, 1,2-benzenediol (catechol) and 2-methoxyphenol (guaiacol) are representative of relevant families of compounds in bio-oils such as ketones, aldehydes and phenols (among these, mainly guaiacols and catechols) [32,33]. Acetic acid, levoglucosan and acetol are present in remarkable concentrations in the bio-oil obtained from pyrolysis of pine sawdust [26,34]. The study of the catalyst behavior in the SR of ethanol is interesting because it may be cofed with bio-oil for its stabilization and because the SR of bio-oil/bio-ethanol mixture (BO + E) is an interesting route for sustainable $H_2$ production from two biomass derived feeds [35].

### 2.2. Catalyst

The catalyst precursor (Ni-Al spinel, $NiAl_2O_4$) was prepared by co-precipitation method with a nominal Ni content of 33 wt% from Ni $(NO_3)_2{\cdot}6H_2O$ and $Al(NO_3)_3{\cdot}9H_2O$ with a $NH_4OH$ 0.6 M solution as a precipitating agent. The precipitation was carried out at 25 °C until the pH was fixed at 8. After aging for 30 min, the precipitate was filtered, washed with distilled water to remove the ammonium ions and dried at 110 °C for 24 h. Lastly, the catalyst was calcined at 850 °C for 4 h [30].

The physical properties of the fresh catalyst and deactivated samples (BET surface area, pore volume and mean pore diameter), were characterized by adsorption–desorption of $N_2$ in a Micromeritics ASAP 2010. Temperature Programed Reduction (TPR) was carried out in a Micromeritics AutoChem 2920 for determining the reducibility of the metal species. The amount and nature of coke deposited on spent catalyst samples has been determined by Temperature Programed Oxidation (TPO) in a TA-Instruments TGA-Q5000IR thermobalance, coupled in line with a mass spectrometer (Thermostar Balzers instrument) for monitoring the signal of $CO_2$. The coke content has been quantified from the $CO_2$ spectroscopic signal, due to Ni oxidation during combustion process masks the thermogravimetric signal in samples with low coke content [30]. The X-Ray Diffraction (XRD) analysis of the reduced fresh and spent catalysts was carried out in a Bruker D8 Advance diffractometer with a CuKα1 radiation, from 10° to 80° with step of 0.04° in 2θ and measurement time of 103 min. The scanning electron microscopy images of the fresh or spent catalysts were taken with a Hitachi S-4800 N field emission gun scanning electron microscope (FEG-SEM), with an accelerating voltage of 5 kV and secondary electron detector (SE-SEM) and a Hitachi S-3400 N microscope with an accelerating voltage of 15 kV, using a backscatter electron detector (BSD-SEM). The transmission electron microscopy (TEM) images were obtained in a Phillips CM-200 microscope using an accelerating voltage of 200 kV. The Raman spectra were carried out in a Renishaw InVia confocal microscope using an excitation wavelength of 514 nm, taking a spectrum in several areas of the sample for assuring reproducibility.

The $N_2$ adsorption–desorption isotherm and the BJH pore distribution of the fresh-reduced catalyst are shown in Figs. S1a and S1b, respectively, in the Supporting Information. An isotherm of type IV according to the IUPAC classification is observed in Fig S1a, which is associated with capillary condensation taking place in mesopores, with a hysteresis of the type H2, attributed to a difference in mechanism between condensation and evaporation processes occurring in pores with narrow necks and wide bodies (often referred to as 'ink bottle' pores). The BET surface are, pore volume and mean pore diameter for the fresh-reduced catalyst (Table 1) are 65.1 $m^2/g$, 0.24 $cm^3/g$ and 13.1 nm, respectively. The TPR profile of the fresh catalyst (Figure S1c) has a maximum $H_2$ uptake at 760 °C, corresponding to the reduction of Ni species incorporated in the $NiAl_2O_4$ spinel structure [30,36]. The XRD pattern of the fresh catalyst prior reduction (black curve in Figure S1d) shows intense peaks at $2\theta = 37.2$, 45.2 and 65.7° corresponding to the cubic structure of $NiAl_2O_4$ spinel, whereas the XRD of the fresh-reduced catalyst (blue curve in Figure S1d) shows peaks corresponding to $Ni^0$ (diffraction angle at 44.5° in (1 1 1) plane, 51.8° in (2 0 0) plane and 75.5° in (1 1 0) plane, JCPDS n° 00–004-0850) and $Al_2O_3$ (37.3°, 45.6° and 66.8°, JCPDS n° 01–077-0396). This result indicates that the reduction treatment (at 850 °C for 4 h) completely converted $NiAl_2O_4$ spinel into reduced Ni crystals supported on $Al_2O_3$ ($Ni/Al_2O_3$), as previously reported [36]. The mean Ni crystal size in the reduced catalyst (calculated with the Debye-Scherrer equation using the diffraction peak at $2\theta = 52°$) is 9 nm (Table 2).

### 2.3. Reaction equipment, operating conditions and reaction indices

Runs have been carried out in an automatized reaction system (MicroActivity-Reference, PID Eng & Tech,) that has been described in detail elsewhere [37], with a fluidized bed reactor. The catalyst (with particle size of 150–250 μm to avoid internal diffusional limitations) is mixed with inert solid (SiC, 37 μm particle size) in order to ensure good fluid dynamic behaviour of the catalytic bed (inert/catalyst mass ratio > 8/1).

Prior to each steam reforming reaction, the catalytic bed is reduced in-situ by using $H_2$-$N_2$ flow (10 vol% of $H_2$) at 850 °C for 4 h, thus forming the active $Ni^0/Al_2O_3$ catalyst. The operating condition for the kinetic runs have been: atmospheric pressure; 600 and 700 °C, that are suitable for attaining high conversion in the SR of bio-oil; space time of 0.034 $g_{catalyst}$ h/$g_{oxygenate}$ in order to favor catalyst deactivation by coke formation during not excessively long runs (of 5 h duration); steam-to-carbon (S/C) molar ratio of 3 (except for levoglucosan, with S/C = 6 due to its low water solubility), which is suitable for promoting WGS reaction (necessary to enhance $H_2$ yield) but without excessive penalty of energy requirements. This S/C ratio has been set by co-feeding water (307 Gilson pump) with the feed (injection pump Harvard Apparatus 22). The reaction products were analysed in a Micro GC Varian CP-490 connected in-line to the reactor through an insulated line (130 °C) to avoid condensation of the products. The gas chromatograph is equipped with three analytic channels: molecular sieve MS5 for quantifying $H_2$, $O_2$, $N_2$, $CH_4$ and CO; PPQ column for light hydrocarbons ($C_2$-$C_4$), $CO_2$ and water; and Stabilwax for oxygenated compounds ($C_{2+}$) and water.

In order to quantify the results, the following reaction indices were used:

$$Carbon\ conversion\ to\ gases: X = \frac{F_{out,\ gas}}{F_{in}} \quad (11)$$

where $F_{out,gas}$ is the molar flow rate of the total carbon in gaseous product ($CO_2$, CO, $CH_4$ and light hydrocarbons, in C units contained) at the reactor outlet, and $F_{in}$ is the molar flow rate of the oxygenate at the reactor inlet in C units contained.

$$H_2\ yield: Y_{H_2} = \frac{F_{H_2}}{F^o_{H_2}} \quad (12)$$

where $F_{H2}$ is the $H_2$ molar flow rate in the product stream and $F^o_{H_2}$, is the stoichiometric molar flow rate, which is calculated as $(2n + m/2 - k)/n\ F_{in}$, according to the global stoichiometry for the SR of each oxygenate ($C_nH_mO_k$) (including the WGS reaction) (Eq. (3)).

**Table 1**
Physical properties of the fresh-reduced catalyst and of spent catalyst samples, coke content ($C_c$, wt%) and average coke formation rate ($r_c$, $g_{coke}/(g_{cat}\ h)$) in the SR of the different oxygenates.

| Sample* | $S_{BET}$, $m^2/g$ | $V_{pore}$, $cm^3/g$ | $d_{pore}$ (BJH), nm | $C_c$, wt% | $r_c$ g/(g h) |
|---|---|---|---|---|---|
| Fresh-reduced | 65.1 (±0.63) ** | 0.24 (±0.01) ** | 13.1 (±0.59) ** | | |
| AA-600 | 224 | 0.24 | 6.8 | 505 | 0.843 |
| AA-700 | 125 | 0.34 | 13.4 | 22.1 | 0.034 |
| AD-600 | 215 | 0.27 | 7.8 | 222 | 0.443 |
| AD-700 | 70 | 0.25 | 13.9 | 2.40 | 0.005 |
| E-600 | 266 | 0.44 | 11.1 | 1500 | 2.001 |
| E-700 | 152 | 0.34 | 10.9 | 35.9 | 0.075 |
| AT-600 | 201 | 0.28 | 8.5 | 207 | 0.414 |
| AT-700 | 65 | 0.23 | 15.7 | 1.70 | 0.003 |
| A-600 | 199 | 0.27 | 8.7 | 989 | 1.974 |
| A-700 | 139 | 0.27 | 10.1 | 104 | 0.207 |
| C-600 | 147 | 0.46 | 19 | 509 | 1.018 |
| C-700 | 198 | 0.33 | 9.2 | 555 | 1.109 |
| G + E-600 | 85 | 0.25 | 19.7 | 332 | 0.664 |
| G + E-700 | 77 | 0.14 | 8.7 | 1014 | 2.029 |
| L-600 | 83 | 0.25 | 13.7 | 17.6 | 0.035 |
| L-700 | 64 | 0.24 | 15.0 | 0.56 | 0.001 |

* The spent catalyst samples are denoted with the name of oxygenated feed (AA = acetic acid; AD = acetaldehyde; E = ethanol; AT = acetol; A = acetone; C = catechol; (G + E) = guiaiacol + ethanol; L = levoglucosan) and the SR temperature (600 or 700 °C).
** The standard deviations evaluated from 3 repetitions.

**Table 2**
Average $Ni^0$ crystal size (determined with Scherrer equation applied to peak at θ = 51.8°) of fresh-reduced catalyst and spent catalyst samples with low coke content (key for sample names in the footnote of Table 1).

| Sample | $d_{Ni}$, nm |
|---|---|
| Fresh-reduced | 9 (±1)* |
| AA-700 | 10 |
| AD-700 | 9 |
| E-700 | 12 |
| AT-700 | 12 |
| A-700 | 9 |
| L-600 | 17 |
| L-700 | 17 |

* The standard deviation evaluated from 3 repetitions.

## 3. Results

### 3.1. Effect of feed composition on catalyst performance

In order to assess the catalyst activity, selectivity and stability for the different feeds studied, the evolution with time on stream (TOS) of carbon conversion to gas and yield of $H_2$ at 600 and 700 °C is shown in Fig. 1 (acetic acid (a), acetaldehyde (b), ethanol (c), acetol (d) and acetone (e)) and Fig. 2 (catechol (a), mixture guaiacol + ethanol (b) and levoglucosan (c)).

At 600 °C, the initial $H_2$ yield (fresh catalyst) varies between 42 % (for acetone, Fig. 1e) and 61 % (for acetaldehyde, Fig. 1b), with similar values (near 50 %) for the rest of oxygenates, thus evidencing similar reactivity at this temperature. The increase in temperature up to 700 °C enhances the carbon conversion to gas and $H_2$ yield at zero time on

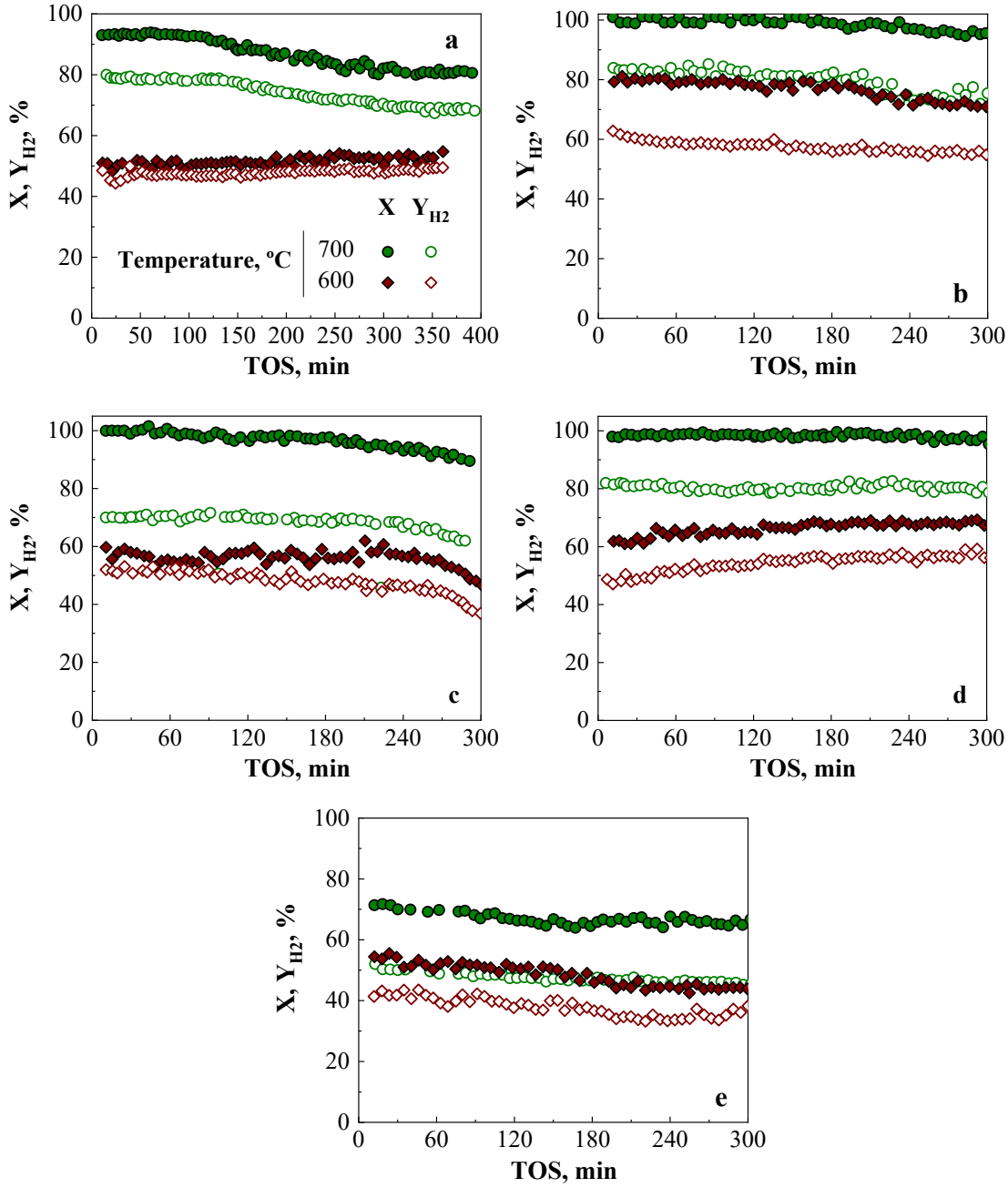


**Fig. 1.** Evolution with time on stream (TOS) of carbon conversion to gas (full markers) and $H_2$ yield (empty markers) in the SR of the light oxygenate compounds: acetic acid (a), acetaldehyde (b), ethanol (c), acetol (d) and acetone (e).

stream in the SR of all oxygenates, with this increase being more significant for acetaldehyde, ethanol and acetol (almost 100 % conversion), and also for acetic acid and catechol (around 93 % conversion). However, it is less noticeable for the guaiacol + ethanol mixture, acetone and levoglucosan, thus evidencing the lower reactivity towards SR reactions at high temperature of the latter oxygenates. The low increase with temperature of the carbon conversion for the guaiacol + ethanol mixture (Fig. 2b), compared to that obtained with ethanol (Fig. 1c), gives evidence of a low effect of temperature for guaiacol, whose reactivity for SR reactions is noticeably lower than that of ethanol, acetic acid, acetaldehyde, acetol and catechol. Moreover, the initial $H_2$ yield in the SR of ethanol at 700 °C (70 %) is lower than that obtained with the other oxygenates (around 80 %), in spite of its high carbon conversion (100 %). This result reveals the higher selectivity of the catalyst for $H_2$ forming reactions (steam reforming and WGS) in the SR of acetic acid, acetol and acetaldehyde compared to ethanol, whose reforming produces significant $CH_4$ formation (not shown). The high $H_2$ yield (80%) obtained in the SR of levoglucosan at 700 °C, in spite of its incomplete carbon conversion, should be attributed to the high S/C ratio used in the SR of this oxygenate (6), that significantly promotes WGS reaction.

Regarding the stability of the catalyst, overall, the conversion and $H_2$ yield remain constant or even increase (for acetic acid (Fig. 1a), acetol (Fig. 1d) and catechol (Fig. 2a)) at 600 °C and slightly decrease with TOS at 700 °C in the SR of all the studied oxygenates, except for guaiacol + ethanol mixture. The increase in conversion and $H_2$ yield with TOS can presumably be explained by the formation of a remarkable amount of filamentous coke (as shown later), which leads to an improved Ni dispersion and better accessibility of reactants due to the tip-growth

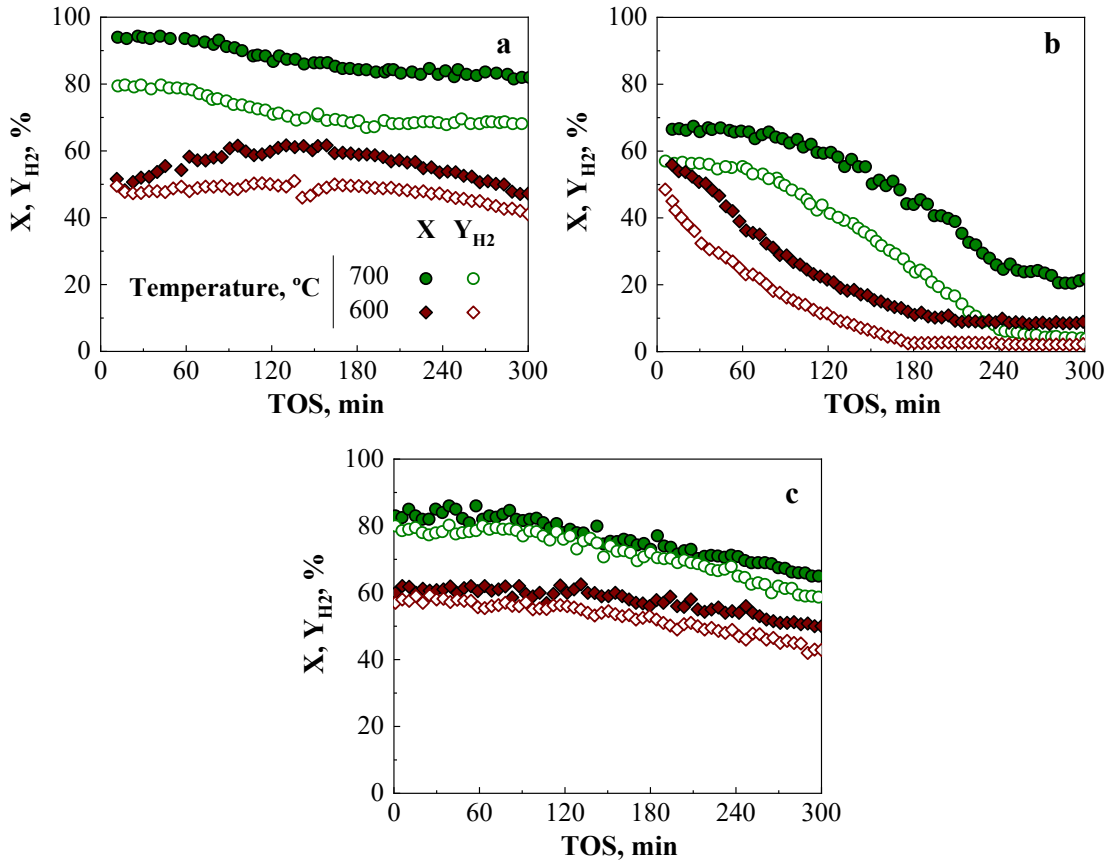


**Fig. 2.** Evolution with TOS of carbon conversion to gas (full markers) and hydrogen yield (empty markers) in the SR of the heavy oxygenate compounds: catechol (a), guaiacol + ethanol mixture (b), and levoglucosan (c).

mechanism of carbon filaments [38]. Conversely, in the SR of the guaiacol + ethanol mixture (Fig. 2b) there is a fast decrease in conversion and $H_2$ yield at both 600 and 700 °C, until the values corresponding to the thermal reaction routes (in the absence of catalyst) are reached. Therefore, this result evidences a much faster deactivation rate of the catalyst in the SR of this mixture than for rest of the oxygenates studied.

### 3.2. Characterization of deactivated catalyst samples

In order to identify the causes responsible for the deactivation of $NiAl_2O_4$ catalyst, and for a better understanding of its deactivation behavior in the SR of the different oxygenates, a thorough characterization of the spent catalyst samples has been performed, by using complementary techniques, that include TPO, SEM and TEM images, XRD, TPR, Raman spectroscopy and $N_2$ adsorption–desorption. These techniques have allowed determining the amount, nature, morphology and structure of the coke deposited in the catalyst, as well as the changes in the metal sites and porous structure of the catalyst. It should be noted that Ni oxidation was ruled out as deactivation cause, as no significant reduction peaks were observed in the $H_2$-TPR profiles of selected deactivated catalyst samples (results not shown here), thus indicating the absence of oxidized species. This is an expected result, which was previously observed in the oxidative steam reforming (OSR) of raw bio-oil with this type of catalyst [39], and it is due to the highly reducing environment in the SR reaction, with a high $H_2$ content. The results of the rest of characterization techniques are presented in the following sections. The spent catalyst samples have been denoted as X-N, where X identifies the oxygenate feed (AA = acetic acid; AD = acetaldehyde; E = ethanol; AT = acetol; A = acetone; C = catechol; (G + E) = guiaiacol + ethanol; L = levoglucosan) and N is the SR temperature (600 or 700 °C).

#### 3.2.1. TPO analysis

Figs. 3 and 4 show the TPO profiles of the deactivated catalysts used in the SR of the oxygenates at different temperatures, obtained from the spectroscopic signal of $CO_2$ released during coke combustion (as explained in section 2.3). These results provide qualitative information on the nature and/or location of the coke in the structure of the catalyst [40]. Several authors differentiate the amorphous and filamentous coke contents of coke deposited on Ni catalysts by deconvolution of the TPO profiles. Thus, Hu et al. [41], relate each type of coke to one of the two peaks of the TPO, so that the amorphous/paraffinic coke burns at lower temperature than the graphitic/filamentous coke. This identification of the two types of coke allowed verifying that with the addition of Fe there is a higher attenuation of the deposition of the graphitic/filamentous coke in the Fe-Ni/$Al_2O_3$ catalysts used in the steam reforming of toluene. The same authors characterize the coke over a Ni/α-$Al_2O_3$ catalyst in the steam reforming of two hydrocarbons (toluene and methylnaphthalene) and two oxygenates (phenol and ethanol) distinguishing amorphous coke from carbon nanotubes (CNTs), whose combustion is identified with the peak at higher combustion temperature [42]. Subsequently, these authors have verified the relevant effect of the steam reforming temperature (in the 500–800 °C range) on the content of the two types of coke and on the quality of the CNTs, proving the existence of a maximum of both at 650 °C [43]. The identification of these two types of coke of different nature by deconvolution of coke combustion TPO profiles was also used to quantify the formation of CNTs on Ni catalysts from the volatiles from polyolefins pyrolysis [44].

The size and location of combustion peaks in Figs. 3 and 4 evidence differences in the amount and nature of coke deposited with the different oxygenates and at different temperature. Noticeably, in the TPO profiles of Figs. 3 and 4 there is apparently a unique combustion

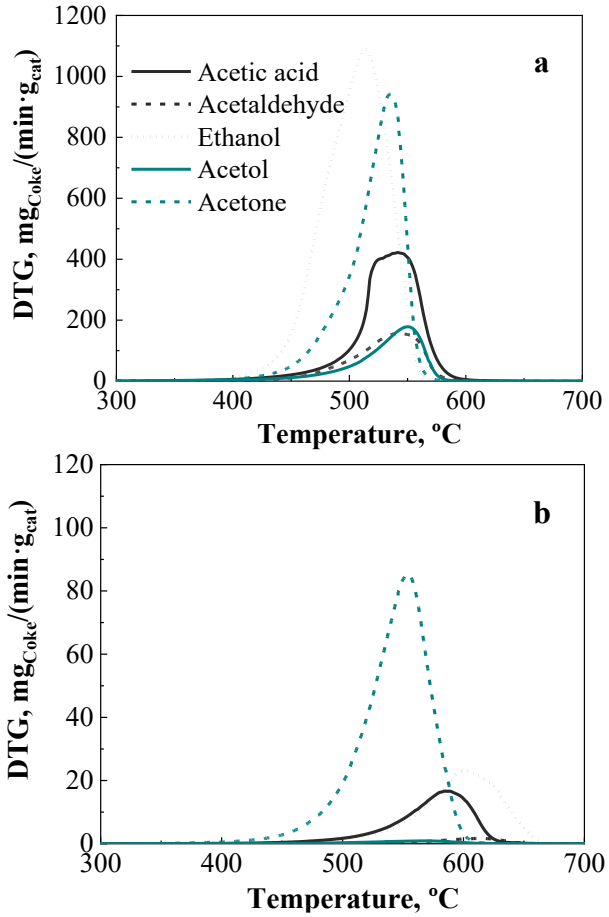


**Fig. 3.** TPO profiles of the catalyst used in the SR at 600 °C (a) and 700 °C (b) of the light non-phenolic oxygenates.

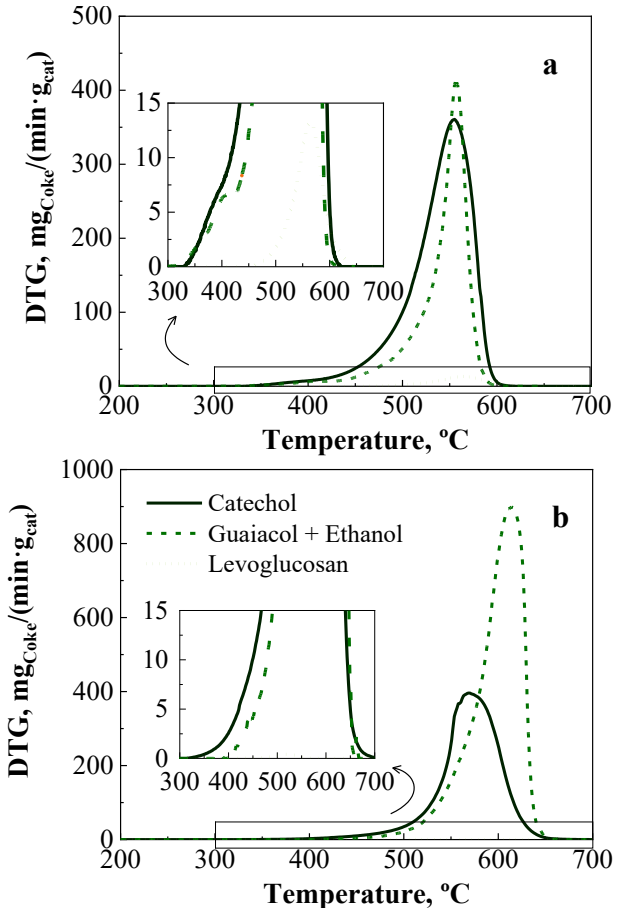


**Fig. 4.** TPO profiles of the catalyst used in the SR at 600 °C (a) and 700 °C (b) of the phenolic oxygenates and levoglucosan.

peak, with maximum in the 500–550 °C range for the SR at 600 °C. This maximum shifts towards higher combustion temperature for the catalyst used in the SR at 700 °C, which suggests that the coke evolves into a more condensed and graphitic-like structure, with lower H/C ratio, and therefore, a higher combustion temperature is required [40].

A shoulder burning at low temperature is also observed in the TPO profiles for the samples deactivated at 600 °C with catechol and guaiacol + ethanol (Fig. 4), which is more noticeable for the latter, but is not observed in the SR of the non-phenolic oxygenates (Fig. 3). This result confirms the previously reported relevant role of phenolic compounds as precursors of the coke burning at low temperature (deposited near metal sites, causing its partial or total encapsulation), deposited in the SR of bio-oil over this catalyst [8]. Taking into account the similar amount of this coke type deposited for catechol and for the mixture (guaiacol + ethanol), with only 50 wt% of guaiacol, it can be concluded that the latter is more prone to its formation.

The results of TPO profiles also provide information on the content of coke deposited, estimated from the total area under the TPO profiles, because the calculation of coke content from TGA results (Figure S2) is masked by the mass increase due to Ni oxidation. The results of coke content are gathered in Table 1, which also includes the average coke deposition rate, calculated assuming linear coke deposition over the reaction. The coke content notably decreases with reforming temperature in the SR of non-phenolic compounds, but, conversely, it increases in the SR of phenolic compounds (catechol and guaiacol), which suggests a different mechanism of coke formation and evolution for the two groups of compounds. At 600 °C, the amount of coke follows the order: ethanol > acetone > acetic acid ≈ catechol > guaiacol + ethanol > acetaldehyde ≈ acetol > levoglucosan, whereas at 700 °C the order is guaiacol + ethanol > catechol ≫ acetone > ethanol > acetic acid > acetaldehyde > acetol > levoglucosan. It should be noted that S/C ratio used in the SR runs with levoglucosan (S/C = 6), is significantly higher than that used with the rest of oxygenates (S/C = 3), which contributes to the lower coke content obtained with levoglucosan at any temperature.

Comparing the results of Table 1 with the deactivation results (Figs. 1 and 2), it is noteworthy that there is no direct relationship between the amount of coke and the deactivation rate. This result has been also reported in previous works on oxygenates reforming [38,45–49], and is explained by the fact that other characteristics of the coke (morphology, structure and location) have a greater impact on deactivation than its content. In addition, it is observed that with similar TPO profiles in terms of peak position (as is the case of coke for the SR of guaiacol + ethanol and catechol at 600 °C) the deactivation rate is different (much faster in the SR of guaiacol + ethanol). Consequently, although the TPO profile of the coke provides valuable qualitative information on the level of condensation and heterogeneity of the coke, to understand the deactivation of the catalyst it is necessary to complete the information on the coke with other characterization techniques of the deactivated catalyst, which will be shown in subsequent sections.

### 3.2.2. *Physical properties of deactivated catalysts*

The textural properties of fresh and deactivated samples (BET surface area, average pore diameter and pore volume) have been determined by means of $N_2$ adsorption–desorption and are displayed in Table 1. The $N_2$ adsorption–desorption isotherms of spent catalyst samples are shown in Fig. 5 (ethanol and (guaiacol + ethanol) feeds) and Figure S3 of

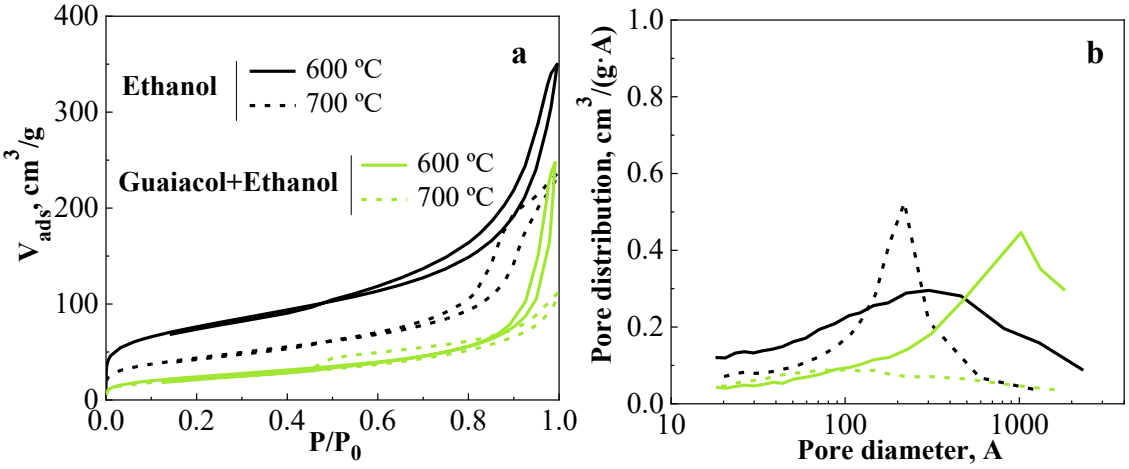


**Fig. 5.** $N_2$ adsorption–desorption isotherms (a) and BJH pore distribution (b) of deactivated catalyst used in the SR of ethanol and guaiacol + ethanol.

Supplementary Information (rest of feeds).

All the samples have isotherm of type IV, but differently to the fresh-reduced catalyst, a H3-type hysteresis cycle is observed for most of the isotherms of catalyst samples used in SR of pure oxygenate compounds, which does not exhibit any limiting adsorption at high $P/P_0$, and is associated to aggregated of plate-like particles giving rise to slit-shape pores [50]. Overall, the shape of the isotherms in Figs. 5 and S3 for spent catalysts does not change with SR temperature, but there are significant differences in the values of textural properties (BET surface area, mean pore diameter and pore volume, gathered in Table 1). In the region of low partial pressures ($P/P_0 \approx 0$), the volume adsorbed in samples of catalyst used in the SR of aliphatic oxygenates and catechol at 600 °C increases noticeably due to the high BET surface area of these samples (which is more than double that of fresh catalyst). This result can be explained by the deposition of porous carbon structures, such as carbon filaments (in agreement with the SEM images shown later, in Figs. 9 and 10), and is consistent with the high stability observed in the SR at 600 °C of these oxygenates. In the samples of catalyst used at 700 °C and with the lowest values of coke deposition (SR of acetaldehyde, acetol and levoglucosan), the physical properties resemble those of the fresh catalyst. On the other hand, the significantly lower total volume adsorbed at high pressures ($P/P_0 \approx 1$) in the sample of the catalyst used in the SR of (guaiacol + ethanol) mixture at 700 °C (Fig. 5a) evidences the partial blockage of the mesopores, thus causing a decrease in BET surface area and mean pore volume (in spite of a high presence of carbon filaments). This partial blockage of the porous structure would contribute to a rapid deactivation, as observed in the SR at 700 °C of this feed (Fig. 2b).

### 3.2.3. *Metallic and structural properties of spent catalyst*

The XRD was carried out to analyze the crystalline structure of the catalyst and of the coke, and also to determine the average size after reaction of Ni metal crystals, by means of Debye-Scherrer equation, at $2\theta = 51.8°$ ($Ni^0$ (200) plane). Fig. 6 shows the XRD diffractograms of spent catalyst samples used in the SR of oxygenates at 600 °C (graph a) and at 700 °C (graph b). The XRD diffractogram of the fresh catalyst is also shown in Fig. 6 for comparison. The same diffraction peaks as in the fresh-reduced catalyst are observed in the spent catalyst samples. Therefore, the presence of NiO is not detected, in agreement with $H_2$-TPR results, which corroborates the high reducing capacity of the reaction medium to keep the active metal in a reduced state.

Moreover, the XRD pattern of most of the spent catalysts shows the presence of a broad peak at a diffraction angle $2\theta = 26°$, which corresponds to high crystallinity cokes (graphite carbon), a characteristic peak usually identified in catalysts used in the steam reforming of pure

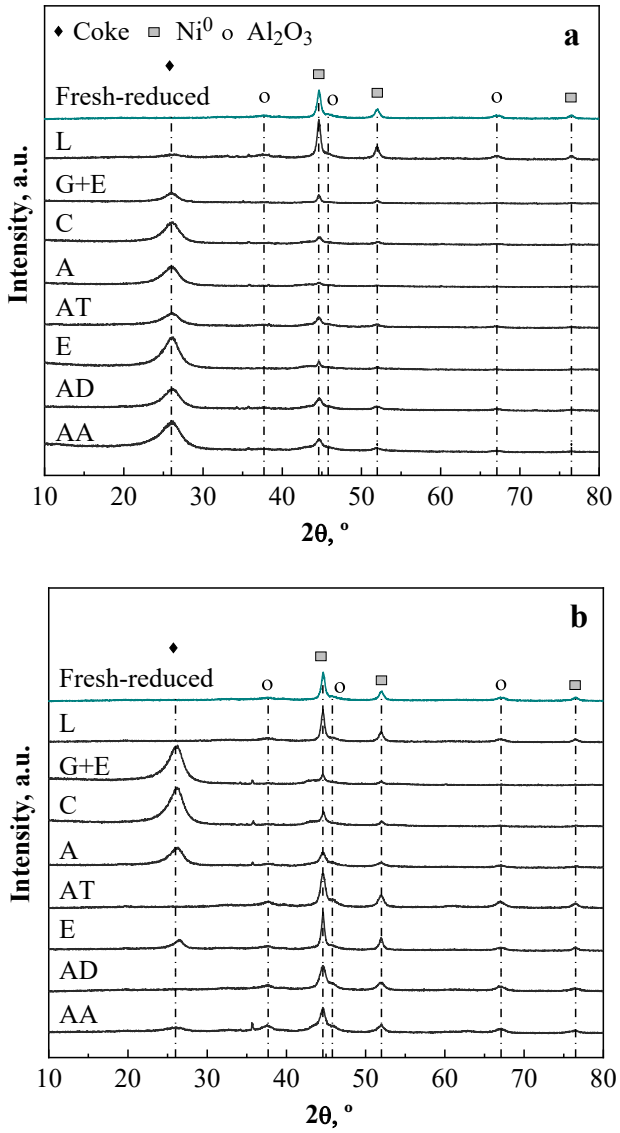


**Fig. 6.** XRD diffractograms of fresh-reduced catalyst and used in the SR of oxygenates at 600 °C (a) and 700 °C (b).

oxygenate compounds (or some mixtures), such as ethanol [51], acetone [52] or acetic acid [53]. The intensity of this peak is in a reasonable agreement with carbon amounts (Fig. 5). Thus, its intensity is high for all the samples deactivated at 600 °C, except for levoglucosan, and for the samples deactivated at 700 °C with phenolic compounds or acetone in the feed, but it is not observed for levoglucosan, acetaldehyde and acetol, due to their low coke content (<3%). Nevertheless, there is not a linear relationship between the intensity of this peak and the amount of coke, which is consequence of differences in the crystallinity level of the different coke deposits.

The calculated average values of $Ni^0$ particles for fresh-reduced and spent catalysts are gathered in Table 2. It should be noted that the calculation is possible only with low-moderate coke content (below 120 wt%), because a high coke content hinders the measurement of metal crystal size from XRD diffractograms (as it masks the $Ni^0$ diffraction peaks). The values of average size of $Ni^0$ crystallites of all used catalysts in Table 2 are around that of fresh catalyst (9 nm), except for SR of levoglucosan, that slightly increases. This moderate sintering of $Ni^0$ crystals could be the responsible of the moderate deactivation rate observed in the SR of levoglucosan (Fig. 2c), in spite of the low coke content deposited in these experiments (Fig. 5).

### 3.2.4. Morphology and location of coke

Figs. 7 and 8 show the BSD-SEM images for the catalyst used in the SR of oxygenates at 600 and 700 °C, respectively. The BDS-SEM images allow determining the presence of some type of elements on the external

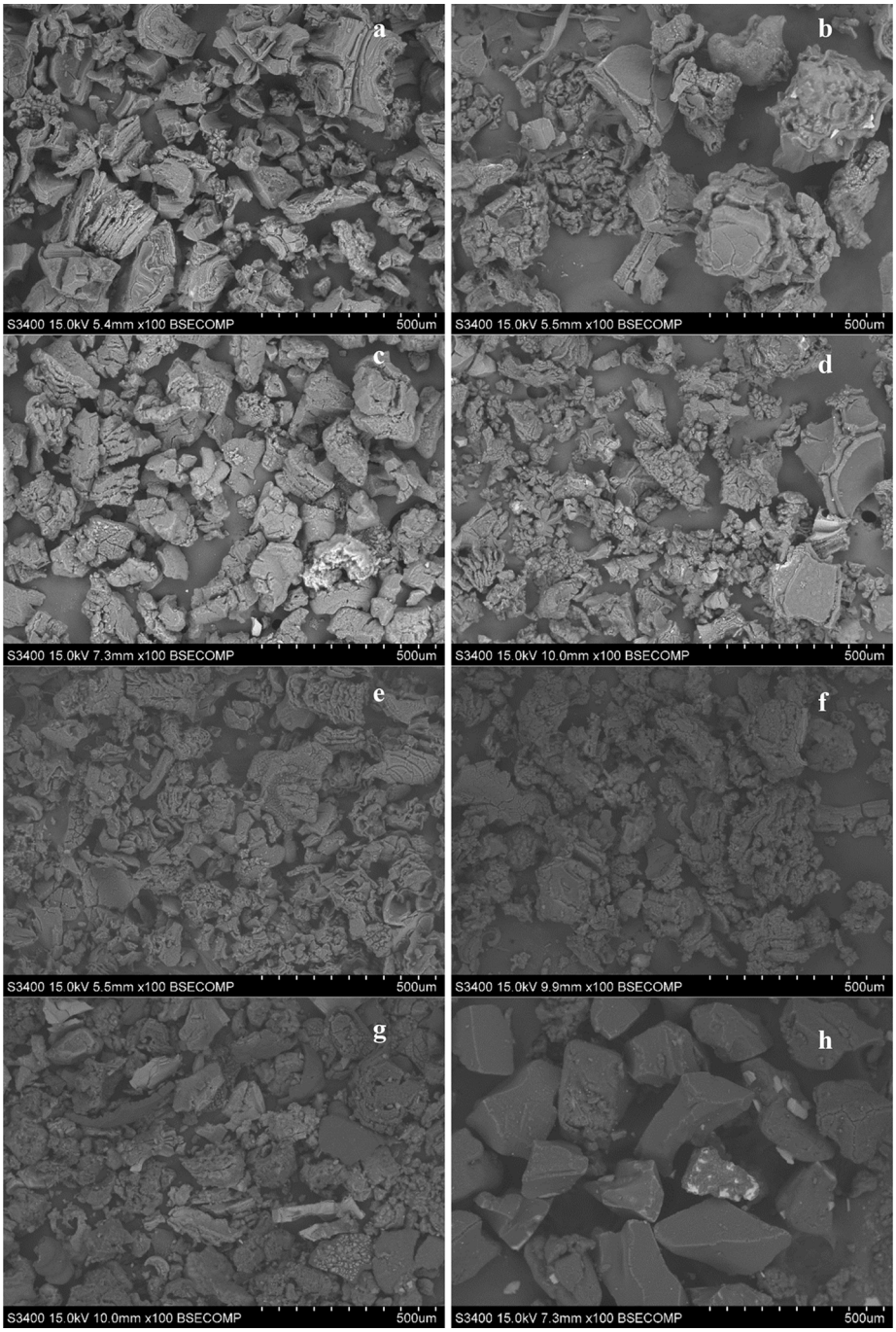


**Fig. 7.** BSD-SEM images of the catalysts used in the SR of acetic acid (a), acetaldehyde (b), ethanol (c), acetol (d), acetone (e), catechol (f), guaiacol + ethanol (g) and levoglucosan (h) at 600 °C.

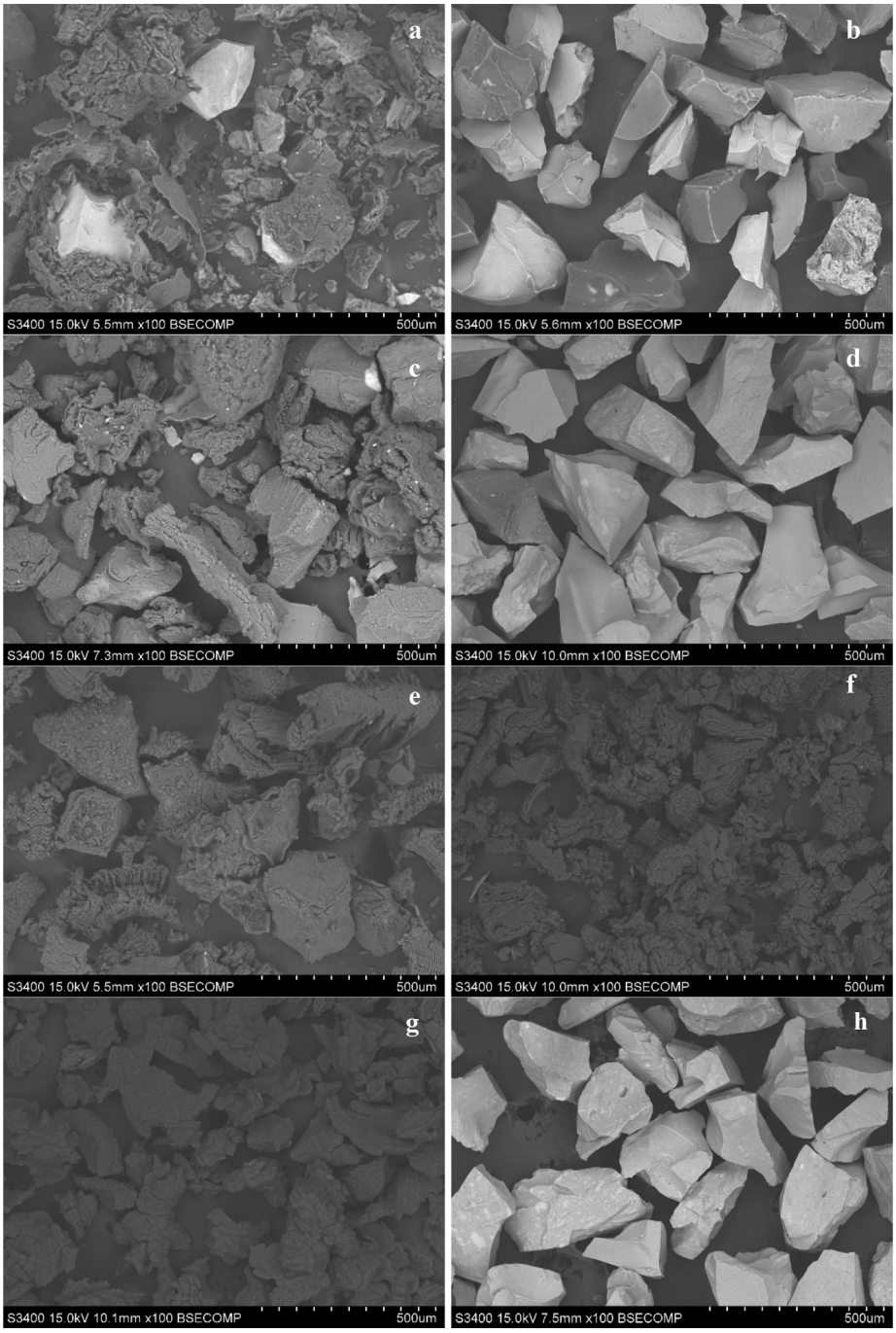


**Fig. 8.** BSD-SEM images of the catalysts used in the SR of acetic acid (a), acetaldehyde (b), ethanol (c), acetol (d), acetone (e), catechol (f), guaiacol + ethanol (g) and levoglucosan (h) at 700 °C.

surface of the particles based on the brightness intensity [47]. Thus, the high brightness intensity of the fresh catalyst (Figure S4) indicates the presence of heavy elements (Ni and Al) constituting the catalyst phases (Ni crystals and $Al_2O_3$). In contrast, the particles of the spent catalysts are generally homogeneous and exhibit a low brightness intensity (dark appearance), which indicates the majority presence of coke on the particle external surface. However, the catalyst used in the SR of levoglucosan at 700 °C (Fig. 8h) shows an homogeneous high brightness intensity, similar to that of the fresh catalyst, which confirms the very low coke deposition observed in the TPO results. On the other hand, the catalyst used in the SR of acetaldehyde at 700 °C (Fig. 8b) shows heterogeneous particles, some with high brightness intensity and others with a dark appearance, which is indicative of the heterogeneous coke deposition.

Additionally, these images also show differences in the particle shapes and textures that can be correlated with the coke content (Table 1). When the coke content is low (below 20 wt%), the particle shape of the spent catalysts (SR of levoglucosan at 600 °C (Fig. 7h) and acetaldehyde, acetol and levoglucosan at 700 °C (Fig. 8b, 8d and 8 h, respectively)) is similar to that of the fresh catalyst, being irregular with a smooth surface and sizes in between 150 and 250 μm (original catalyst particle size). When the coke content is moderately high (between 20 and 120 wt%), the particle texture of the spent catalysts (SR of acetic acid, ethanol and acetone at 700 °C (Fig. 8a, 8c and 8e, respectively)) changes to a rough surface keeping the original catalyst particle size. In particular, the catalyst used in the SR of acetic acid at 700 °C (Fig. 8a)

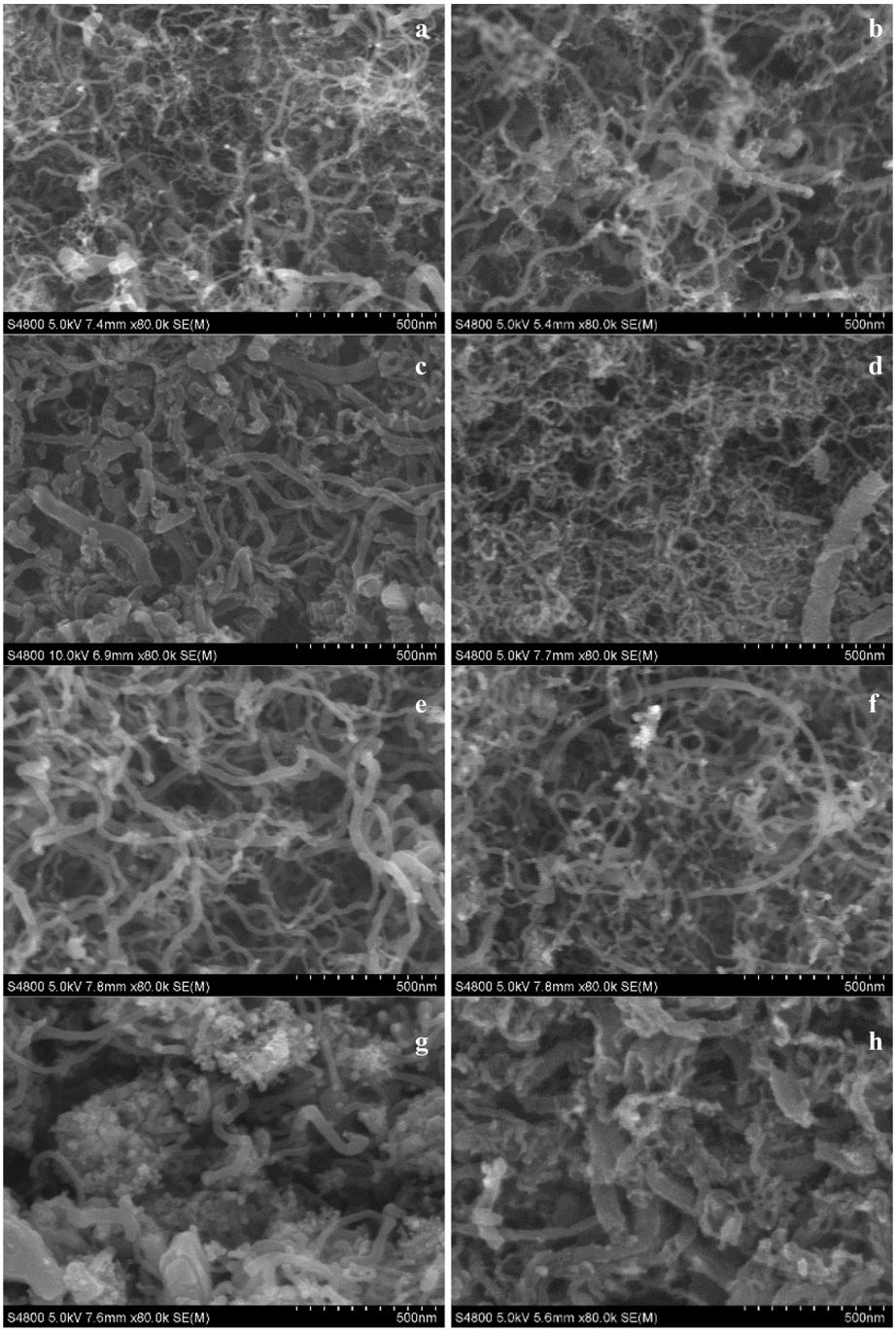


**Fig. 9.** SE-SEM images of the catalysts used in the SR of acetic acid (a), acetaldehyde (b), ethanol (c), acetol (d), acetone (e), catechol (f), guaiacol + ethanol (g) and levoglucosan (h) at 600 °C.

shows bare catalyst particles with fragments of coke shells, evidencing the low mechanical strength of the superficial coke shells. When the coke content is high (above 200 wt%), the particles of the spent catalysts (rest of the experiments) have a rough surface and are remarkably smaller than the original catalyst particle size, which may indicate a collapse of the catalyst particles due to the excessive coke growth.

Figs. 9 and 10 show the SE-SEM images of the spent catalyst surfaces. In general, at 600 °C (Fig. 9), the images show the formation of carbon filaments from all the model compounds with different characteristics (heterogeneous in size and texture). In particular, the carbon filaments from SR of ethanol (Fig. 9c) show a rough surface, indicating the growth/deposition of carbon along the filaments. Additionally, the formation of an amorphous carbon phase is observed in the catalyst used in the SR of guaiacol + ethanol (Fig. 9g), and in comparison with the catalyst used in the SR of ethanol (Fig. 9c), this carbon phase is inferred to be formed from guaiacol. At 700 °C (Fig. 10), the SE-SEM images clearly show the predominant formation of carbon filaments from acetic acid, acetaldehyde, ethanol, acetone and catechol. The aforementioned peculiar feature of the carbon filaments from ethanol is highly noticeable at this temperature (Fig. 10c), indicating the growth/deposition of carbon along the filaments is favored. A second carbon phase in between the filaments is observed in the SR of guaiacol + ethanol (Fig. 10g), probably due to the formation of pyrolytic carbon from guaiacol (as explained in discussion section) which is more predominant on some regions of the catalyst surface (Figure S5). On the other hand, the surface of the spent catalysts with low coke content (SR of acetol and

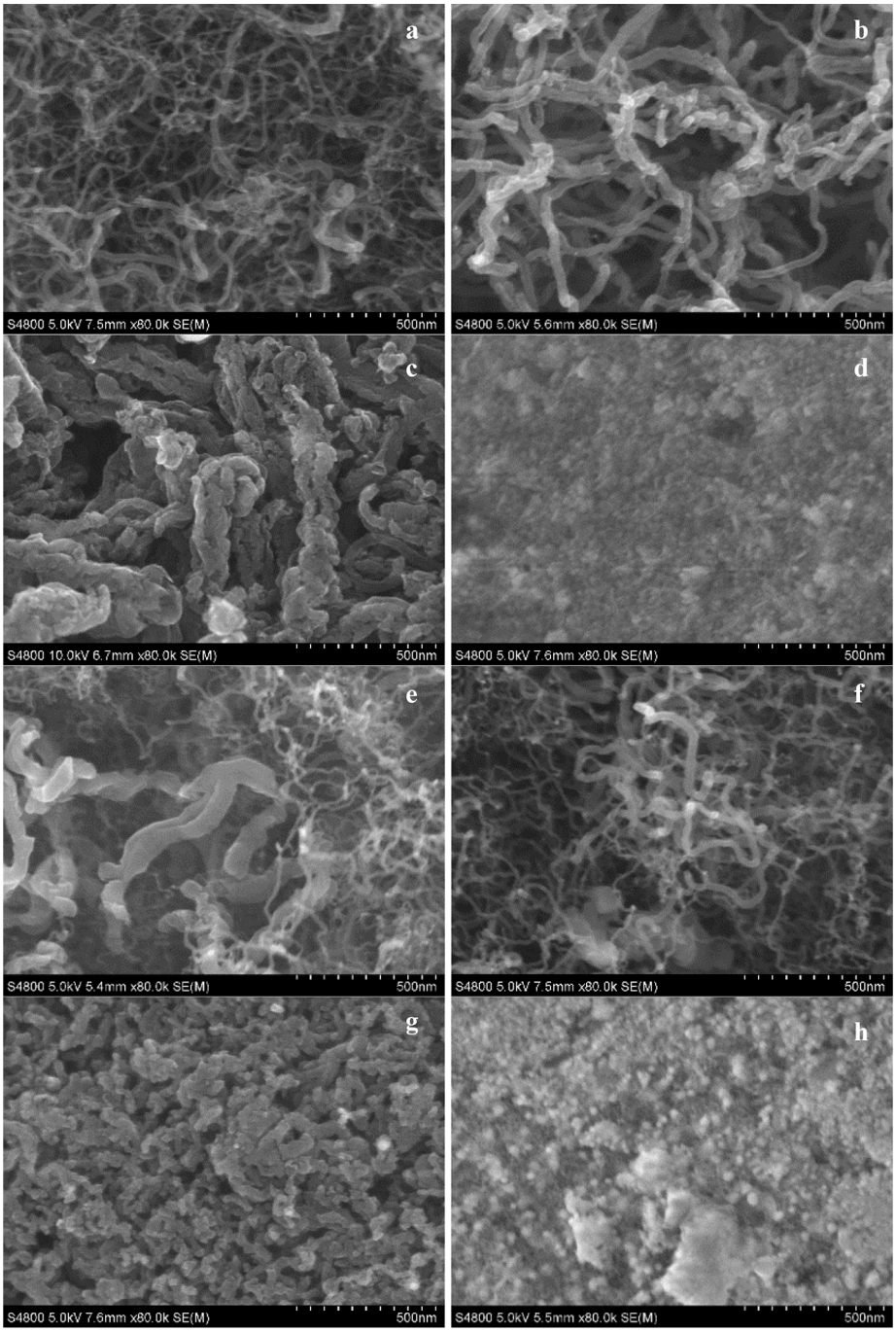


**Fig. 10.** SE-SEM images of the catalysts used in the SR of acetic acid (a), acetaldehyde (b), ethanol (c), acetol (d), acetone (e), catechol (f), guaiacol + ethanol (g) and levoglucosan (h) at 700 °C.

levoglucosan, Fig. 10d and 10 h, respectively) resembles that of the fresh catalyst, which confirms no significant coke deposition.

To study the location of coke on the catalyst surface, Figure S6 shows contrasts of BSD-SEM and SE-SEM images for selected spent catalyst samples. In the spent catalyst with carbon filaments, Ni crystals are often visualized on the tip of the filaments, but not for all the cases. Interestingly, for the catalyst used in the SR of acetic acid at 600 °C (Figure S6c), a large filament was captured showing various Ni crystals along it, which indicates that various Ni crystals may be involved in the growth of large filaments. To complement these observations, selected spent catalyst samples were also analyzed using TEM, and the images (Figures S7 and S8) evidence the formation of hollow carbon filaments (carbon nanotubes) with thick walls (probably multiwall carbon nanotubes, MWCNT) and the presence of Ni crystals on the tip of or along the filaments with no evidence of sintering. Particularly, the catalysts used in the SR of guaiacol + ethanol at 600 and 700 °C (Figure S7) showed two carbon phases (amorphous and filaments). The presence of Ni crystals on the tip of the filaments is an expected observation based on the tip growth mechanism commonly described for the formation of carbon filaments on different Ni catalysts used in the SR of oxygenates [38,42,54,55]. It also explains the catalyst stability observed in the experiments for the SR of acetic acid, acetaldehyde, ethanol, acetol, acetone, catechol and levoglucosan (Figs. 1 and 2) in spite of the high content of filaments, because Ni crystals are exposed and accessible for the reactants. However, the rapid catalyst deactivation observed for the SR of guaiacol + ethanol in Fig. 2b is associated to the formation of a

second carbon phase at 600 and 700 °C, which is also observed in the SR of raw bio-oil [31,34]. This carbon phase is formed from guaiacol and has an amorphous nature at 600 °C and a pyrolytic nature at 700 °C based on the coke combustion characteristics (Fig. 4a and 4b, respectively).

### 3.2.5. Structural properties of coke

Fig. 11 shows the Raman spectra of selected spent catalyst samples to further study the structural properties of coke. All the samples show the typical D (corresponding to disordered aromatic structures, at ~ 1343 $cm^{-1}$) and G (corresponding to condensed, ordered or graphitic aromatic structures, ~1589 $cm^{-1}$) bands as commonly found for various carbon structures, and the corresponding second-order bands in the 2500–3500 $cm^{-1}$ region (Figure S9) [31,56,57]. At 600 °C, the G and D bands have similar features for all the spent catalyst samples (SR of ethanol, acetol, guaiacol + ethanol and levoglucosan) with noticeable different intensities for the D band. The intensity ratio between the D and G band ($I_D/I_G$) determined from deconvolution (procedure described in the SI document and results summarized in Table 3) is notoriously higher for the coke formed from the SR of ethanol, and consecutively decreases for the coke corresponding to acetol, levoglucosan and guaiacol + ethanol. At 700 °C, the D and G band features are significantly different. Thus, the coke formed from ethanol has narrow D and G bands, the G band has a shoulder at 1605 $cm^{-1}$ and noticeable higher $I_D/I_G$ ratio. The spectra of the coke formed from levoglucosan present a high noise level, which is coherent with the low coke content determined from the TPO analysis.

Moreover, the Raman spectra mostly correspond to carbon nanotubes (CNT) with different structural qualities, in coherency with the results of SEM and TEM analyses, which revealed the presence of CNT in the catalysts used in the SR of ethanol, acetol, guaiacol + ethanol and levoglucosan at 600 °C and ethanol and guaiacol + ethanol at 700 °C. The spectrum for ethanol at 700 °C is very close to that of MWCNT, exhibiting dominant narrow D and G bands [58–60]. The intensity ratio between the D3 (assigned to amorphous carbon) and G bands ($I_{D3}/I_G$) (listed in Table 3) provides an indicator for measuring the quality of carbon nanotubes [59], indicating that those formed from ethanol at 700 °C would have the highest purity having the lowest $I_{D3}/I_G$ ratio (0.06).

It is also observed that the Raman spectra for the catalyst used in the SR of guaiacol + ethanol at 600 and 700 °C is typical of carbon structures with different degree of order [61], which is in agreement with the formation and deposition of a second carbon phase between the filaments. This result is in agreement with the BSD-SEM (Fig. 8g) and SEM (Fig. 10g) images discussed above. Based on the $I_D/I_G$ ratio, being higher at 700 °C than at 600 °C, the second carbon phase is predominantly amorphous with ordered domains below 2 nm, but it is more structured at 700 °C, which is consistent with the higher combustion temperature observed in the TPO analysis (Fig. 4b). This relationship between TPO and Raman spectroscopic analyses has been also observed for this catalyst used in the SR of raw bio-oil [31], evidencing the formation of carbon filaments and amorphous carbon with different degree of order, which indicates an analogy between coke deposition in the SR of guaiacol and raw bio-oil.

**Table 3**
Raman spectra deconvolution results of the coke deposited on spent catalyst samples (key for sample names in the footnote of Table 1).

| Sample | $FWHM_D$ | $FWHM_{D3}$ | $FWHM_G$ | $I_D/I_G$ | $I_{D3}/I_G$ |
|---|---|---|---|---|---|
| E-600 | 95.0 | 143 | 63.0 | 1.1 | 0.20 |
| E-700 | 58.0 | 65.0 | 45.0 | 1.7 | 0.06 |
| AT-600 | 110 | 138 | 59.0 | 0.98 | 0.21 |
| AT-700 | 95.0 | 138 | 53.0 | 1.0 | 0.20 |
| G + E-600 | 96.0 | 167 | 75.0 | 0.71 | 0.18 |
| G + E-700 | 97.0 | 137 | 56.0 | 0.81 | 0.16 |
| L-600 | 147 | 142 | 57.0 | 0.82 | 0.21 |
| L-700 | 138 | 148 | 53.0 | 0.75 | 0.20 |

FWHM stands for full width at half maximum.

## 4. Discussion

The deactivation of the catalyst in the oxygenates SR can be explained by the steps in Fig. 12, where the nature of the coke is key.

### 4.1. Coke as the main cause of deactivation

The characterization of deactivated catalyst samples (amount and morphology of coke deposits, sections 3.2.1, 3.2.4 and 3.2.5, as well as physical, metallic and textural properties, section 3.2.2 and 3.2.3) has allowed establishing the deactivation causes of the $NiAl_2O_4$ spinel derived catalyst in the SR of the different oxygenates at 600 and 700 °C. Firstly, Ni oxidation has been ruled out as a deactivation cause, due to the absence of reduction peaks (TPR) or $NiO_x$ diffraction peaks (XRD measurements) in all the spent catalysts, which is coherent with the highly reducing atmosphere along the SR reactions, and is in agreement with the results reported for the SR of raw bio-oil [31]. Secondly, Ni sintering does not appear to be a relevant cause of deactivation of this catalyst, since it is not observed a significant increase in the average $Ni^0$ crystal size, except for SR of levoglucosan, where a slight deactivation is

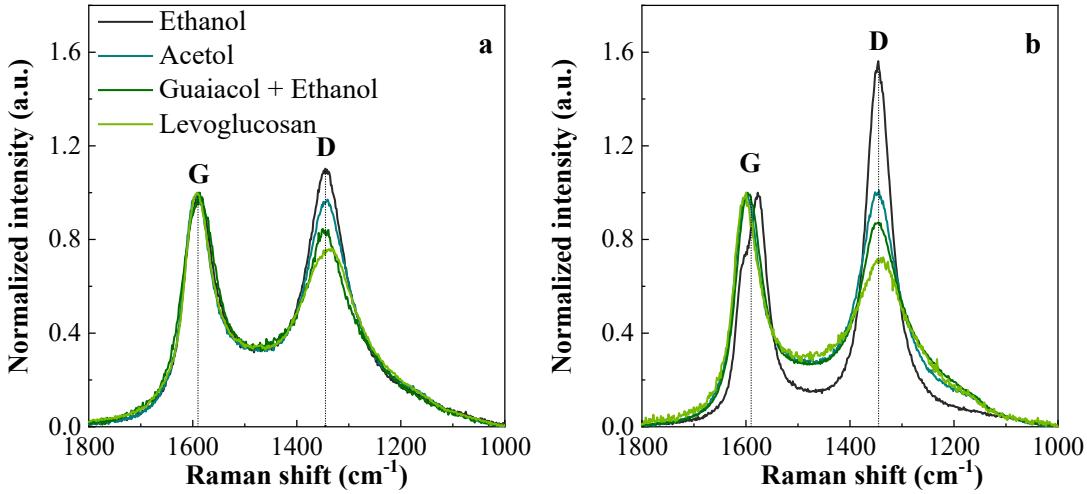


**Fig. 11.** Raman spectra of the catalysts used in the SR of ethanol, acetol, guaiacol + ethanol and levoglucosan at 600 °C (a) and 700 °C (b).

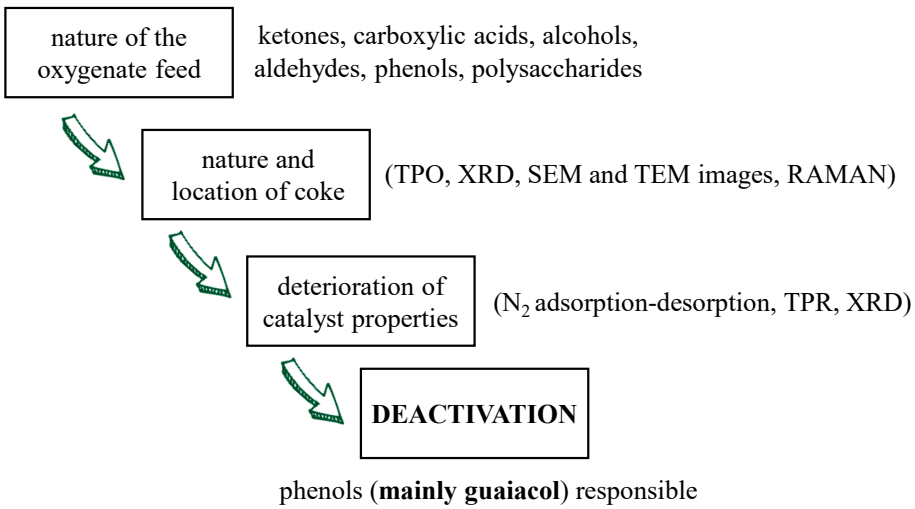


**Fig. 12.** Effect of the oxygenate nature on the deactivation of the $NiAl_2O_4$ spinel derived catalyst in the SR of oxygenates.

observed (Fig. 2c). Nevertheless, a similar moderate Ni sintering has been reported in the SR of raw bio-oil at 700 °C with this catalyst [31], which does not explain the rapid deactivation for this reaction. Consequently, the main cause of the rapid deactivation of the $NiAl_2O_4$ derived catalyst in the SR of bio-oil and of the guaiacol + ethanol mixture must be attributed to coke deposition.

### 4.2. Relevance of coke nature in deactivation

By relating the results of TPO analysis and SEM images of the deactivated samples (sections 3.2.1 and 3.2.4) to the deactivation rate of the catalysts, it has become clear that deactivation is directly related to the nature of the coke, in agreement with previous results in literature for different catalysts [38,45–49]. Thus, a large amount of filamentous coke is deposited in the SR of most of the pure oxygenates studied (especially at 600 °C), but it does not cause a significant impact on the activity of the catalyst. The increase in $S_{BET}$ (Table 1) and the BSD-SEM images (Figs. 7 and 8) for the catalyst used in the SR of oxygenates (such as acetic acid, acetaldehyde, ethanol, acetol and acetone) evidences the deposition of a porous and filamentous coke with contents in the catalyst above 20 wt%, but that does not hinder the access of reactants to metal sites in the reaction time studied. However, for a high time on stream, it can create a slight plug on pores or it may grow as clumps of entangled filaments that encapsulate metal particles [47], which can originate a decrease in activity as that observed at high reaction time in the SR of ethanol (Fig. 1c).

The low values of $S_{BET}$ in the catalyst used in SR of guaiacol + ethanol (only slightly above that of fresh catalyst) is explained by the formation of both i) filamentous coke that is probably stacked on the surface of the catalyst and causes an increase in BET surface area (with high contribution of ethanol to the formation of this type of coke), and ii) an amorphous carbon phase in between the carbon filaments, probably due to the formation of pyrolytic carbon from guaiacol, which is promoted at high temperature, and that clogs the porous structure and contributes to the rapid deactivation observed for the mixture (guaiacol + ethanol) (Fig. 2b). This formation of pyrolytic coke by repolymerization of phenols in bio-oil is well established in the literature [62].

According to the literature, the importance of the properties of the catalyst in the nature of the coke should be pointed out. Thus, Zhang et al. [48], observed the prevalent formation of amorphous coke from guaiacol on $Ni/Al_2O_3$ catalyst, whereas carbon nanotubes are preferentially formed on Ni/SBA-15 catalyst.

### 4.3. Role of the different oxygenates in deactivation

Due to the filamentous nature of coke, the catalyst stability is high in the SR of non-phenolic oxygenates, (Fig. 1), as well as in the SR of catechol (Fig. 2a) and levoglucosan (Fig. 2c). Conversely, the catalyst undergoes complete deactivation after 300 min reaction in the SR of the guaiacol + ethanol mixture at both temperatures studied. Taking into account the high stability observed in the SR of ethanol (Fig. 1c), it can be concluded that guaiacol is the responsible of the rapid catalyst deactivation observed in Fig. 2b.

The origin of long and heterogeneous carbon filaments in the SR of aliphatic oxygenates (Figs. 9 and 10) can be attributed to the reaction of CO (Boudouard reaction, Eq. 9) and $CH_4$ decomposition (Eq. 8) [51,63,64]. As $CH_4$ decomposition is favoured above 750 °C, in the conditions of this study the main origin of this coke is probably the exothermic Boudouard reaction, whose extent is favoured at lower temperature. Moreover, in the SR of ethanol at 600 °C with the same catalyst, the contribution to the formation of filamentous coke by the route of dehydration to ethylene over the acid sites of the $Al_2O_3$ support followed by the ethylene decomposition on the $Ni\text{-}Al_2O_3$ interface has been proved [36]. Also, acetone is an important precursor of filamentous coke [14,65], which can explain the higher amount of coke deposited in the SR of acetone than in the SR of acetic acid.

The formation of filamentous coke is also significant in the SR of the phenolic compounds, as revealed by SEM images (Fig. 9f, 9g, 10f and 10g), and the high combustion peak located at high temperature in the TPO profiles (Fig. 4). But differently to the SR of aliphatic oxygenates, the presence of a small coke fraction burning at low temperature (amorphous and encapsulating coke) is observed in the SR at 600 °C of catechol and more notoriously in the SR of the guaiacol + ethanol mixture (Fig. 4a). For this latter feed, the formation of this amorphous carbon phase could explain the lower amount of filamentous coke deposited at this temperature (Fig. 9g) compared to the SR of ethanol (Fig. 9c). Thus, the formation of encapsulating coke on metal sites hinders the mechanisms of filamentous coke formation, which requires diffusion of C species through Ni metal particles, their precipitation on the base of the Ni crystallite and the formation of a carbon filament growing in size [51,66]. This synergy in the mechanism of formation of each type of coke from each oxygenate makes it difficult to understand the mechanism of coke formation from a complex mixture such as raw bio-oil.

### 4.4. Effect of temperature

The difference in the results of coke amount at 600 and 700 °C can be explained by the effect of temperature on the reactions involved in their formation (mainly Boudouard reaction (Eq. 9) and polymerization reactions) and their elimination (gasification reaction, Eq. (10)). Thus, the polymerization and gasification reactions are favored with the increase in temperature, whereas the Boudouard reaction is disfavored. Consequently, the increase in the reaction rate of gasification and the lower extent of Boudouard reaction explain the sharp reduction of coke amount on the catalyst observed in the SR of aliphatic oxygenates at 700 °C [67]. Nevertheless, in the SR of phenolic oxygenates the coke amount is higher at 700 °C, especially for the guaiacol + ethanol mixture, because guaiacol polymerization (with pyrolytic carbon formation, Fig. 10g) is favored to a greater extent than gasification. A similar result was previously reported for other heavy oxygenates like glucose and m-xylene [14,20].

This effect of temperature on coke formation is very important in the reforming of levoglucosan, where the coke amount is 16.7 wt% at 600 °C and 0.5 wt% at 700 °C. Considering the ease of cracking of this oxygenate [68] it can be understood that the increase in the cracking rate favors the SR of the intermediates to a greater extent than their polymerization, which explains the low coke deposition. The extent of thermal cracking is different for each oxygenate in the bio-oil depending on its functionality, which affects the results of the raw bio-oil SR, and in particular deactivation. Moreover, increasing the temperature above 700 °C also favors the gasification of the coke retained in the catalyst, attenuating its development towards filamentous structures. However, as aforementioned, this strategy has the unfavorable effect of Ni sintering. It should be noted that this problem is minimized with the $NiAl_2O_4$ spinel derived catalyst, which recovers its spinel structure by controlled calcination, recovering the dispersion and size of the $Ni^0$ crystals in successive reaction-reduction-regeneration cycles [30].

### 4.5. Comparison with deactivation in the SR of raw bio-oil

In a previous study of the deactivation of the same $NiAl_2O_4$ spinel derived catalyst in the SR of raw bio-oil [31] was found that the coke is mainly constituted of short and heterogeneous filaments, representing much lower amounts than those formed in this work from aliphatic oxygenates, being remarkable the presence of amorphous and encapsulating coke. Based on the results of the present work, the formation of this coke may be attributed to the high content of guaiacols and catechols, and heavier phenolic compounds in raw bio-oil, whose polymerization significantly inhibits the mechanisms of formation of abundant and long carbon filaments on the catalyst surface from aliphatic oxygenates present in bio-oil.

Consequently, the phenolic compounds have a relevant role in the deactivation of the $NiAl_2O_4$ derived catalyst during the SR of raw bio-oil. Nevertheless, the decrease in carbon conversion [31] is faster than that observed in the SR of the guaiacol + ethanol mixture (Fig. 2b), which evidences the significant contribution of other compounds in bio-oil, most probably heavier phenolic compounds, to the deactivation of the catalyst. Moreover, a synergistic effect of the presence of different compounds in bio-oil (with different functionalities) could also contribute to a more rapid deactivation in the SR of bio-oil than in the SR of each pure oxygenated compound. Consequently, in order to establish a mechanism that faithfully represents the reality of coke formation and catalyst deactivation in the SR of raw bio-oil, the study of pure oxygenated model compounds is not sufficient, but studies of co-feeding of binary mixtures and progressively more complex mixtures are required. However, based on the results of this work, it is advisable to separate the phenolic components from the raw-bio-oil to mitigate the deactivation by coke, although this implies a decrease in the $H_2$ yield and the formation of a byproduct stream.

## 5. Conclusions

The deactivation of the $NiAl_2O_4$ spinel derived catalyst in the SR of oxygenates at 600–700 °C is a consequence of coke deposition, whose effect on the deactivation rate highly depends on the oxygenates nature, which determines the coke nature and its deactivation ability. Thus, the formation of filamentous coke from the aliphatic oxygenates by the Boudouard reaction has a reduced deactivation effect, because it does not blocks the porous structure of $Al_2O_3$. However, the formation of amorphous and Ni-encapsulating coke in the SR of guaiacol leads to a rapid deactivation of the catalyst. The increase in temperature from 600 to 700 °C has low impact on deactivation because it favors the extent of encapsulating coke formation reactions by polymerization but attenuates the formation of filamentous coke by promoting its gasification.

Presumably, in the SR of raw bio-oil a synergy between the mechanisms of coke formation from the different oxygenates present is to be expected. But according to the results of this work, the formation of encapsulating coke from phenolic oxygenates is preferential and inhibits the formation of filamentous coke from aliphatic oxygenates. Consequently, the results of this work can be applied to: i) use guaiacol as oxygenate model to test the stability of new catalysts and adapt the reaction conditions in order to minimizing deactivating coke, and ii) design of pretreatment methods of bio-oil in order to eliminate the guaiacol and phenolic components in order to minimizing the formation of this coke.

## Declaration of Competing Interest

The authors declare that they have no known competing financial interests or personal relationships that could have appeared to influence the work reported in this paper.

## Acknowledgements

This work has been carried out with the financial support of the Ministry of Science and Innovation of the Spanish Government (grant RTI2018-100771-B-I00 funded by MCIN/AEI/10.13039/501100011033 and by "ERDF A way of making Europe"), the European Commission (HORIZON H2020-MSCA RISE 2018. Contract No. 823745) and the Department of Education, Universities and Investigation of the Basque Government (Project IT1645-22, IT1218-19 and PhD grant PRE_2021_2_0147 for L. Landa). The authors thank for technical and human support provided by SGIker (UPV/EHU/ERDF, EU).

## Appendix A. Supplementary data

Supplementary data to this article can be found online at https://doi.org/10.1016/j.fuel.2022.124009.

## References

[1] Setiabudi HD, Aziz MAA, Abdullah S, Teh LP, Jusoh R. Hydrogen production from catalytic steam reforming of biomass pyrolysis oil or bio-oil derivatives: A review. Int J Hydrogen Energy 2020;45:18376–97. https://doi.org/10.1016/j.ijhydene.2019.10.141.

[2] European Commission. Europe's moment: Repair and prepare for the next generation 2020. https://ec.europa.eu/commission/presscorner/detail/en/ip_20_940.

[3] Suleman F, Dincer I, Agelin-Chaab M. Environmental impact assessment and comparison of some hydrogen production options. Int J Hydrogen Energy 2015;40:6976–87. https://doi.org/10.1016/j.ijhydene.2015.03.123.

[4] Lepage T, Kammoun M, Schmetz Q, Richel A. Biomass-to-hydrogen: A review of main routes production, processes evaluation and techno-economical assessment. Biomass Bioenergy 2021;144:105920. https://doi.org/10.1016/j.biombioe.2020.105920.

[5] Arregi A, Lopez G, Amutio M, Artetxe M, Barbarias I, Bilbao J, et al. Role of operating conditions in the catalyst deactivation in the in-line steam reforming of volatiles from biomass fast pyrolysis. Fuel 2018;216:233–44.

[6] Baloch HA, Nizamuddin S, Siddiqui MTH, Riaz S, Jatoi AS, Dumbre DK, et al. Recent advances in production and upgrading of bio-oil from biomass: A critical overview. J Environ Chem Eng 2018;6(4):5101–18.

[7] Xu Q, Feng P, Huang K, Xin S, Wei T, Liao L, et al. Research of the combined reforming of bio-oil model compound for hydrogen production. Environ Prog Sustain Energy 2020;39(2):e13320. https://doi.org/10.1002/ep.13320.

[8] Valle B, García-Gómez N, Arandia A, Remiro A, Bilbao J, Gayubo AG. Effect of phenols extraction on the behavior of Ni-spinel derived catalyst for raw bio-oil steam reforming. Int J Hydrogen Energy 2019;44:12593–603. https://doi.org/10.1016/j.ijhydene.2018.12.057.

[9] Vagia EC, Lemonidou AA. Thermodynamic analysis of hydrogen production via autothermal steam reforming of selected components of aqueous bio-oil fraction. Int J Hydrogen Energy 2008;33:2489–500. https://doi.org/10.1016/j.ijhydene.2008.02.057.

[10] Basagiannis AC, Verykios XE. Influence of the carrier on steam reforming of acetic acid over Ru-based catalysts. Appl Catal B Environ 2008;82:77–88. https://doi.org/10.1016/j.apcatb.2008.01.014.

[11] Zhang L, Yu Z, Li J, Zhang S, Hu S, Xiang J, et al. Steam reforming of typical small organics derived from bio-oil: Correlation of their reaction behaviors with molecular structures. Fuel 2020;259:116214.

[12] Wang Y, Sun K, Zhang S, Xu L, Hu G, Hu X. Steam reforming of alcohols and carboxylic acids: Importance of carboxyl and alcoholic hydroxyl groups on coke properties. J Energy Inst 2021;98:85–97. https://doi.org/10.1016/j.joei.2021.06.002.

[13] Medrano JA, Oliva M, Ruiz J, García L, Arauzo J. Catalytic steam reforming of model compounds of biomass pyrolysis liquids in fluidized bed reactor with modified Ni/Al catalysts. J Anal Appl Pyrolysis 2009;85:214–25. https://doi.org/10.1016/j.jaap.2008.11.025.

[14] Hu X, Lu G. Investigation of the steam reforming of a series of model compounds derived from bio-oil for hydrogen production. Appl Catal B Environ 2009;88:376–85. https://doi.org/10.1016/j.apcatb.2008.10.021.

[15] An L, Dong C, Yang Y, Zhang J, He L. The influence of Ni loading on coke formation in steam reforming of acetic acid. Renew Energy 2011;36:930–5. https://doi.org/10.1016/j.renene.2010.08.029.

[16] Bimbela F, Chen D, Ruiz J, García L, Arauzo J. Ni/Al coprecipitated catalysts modified with magnesium and copper for the catalytic steam reforming of model compounds from biomass pyrolysis liquids. Appl Catal B Environ 2012;119–120:1–12. https://doi.org/10.1016/j.apcatb.2012.02.007.

[17] Wang S, Cai Q, Zhang F, Li X, Zhang L, Luo Z. Hydrogen production via catalytic reforming of the bio-oil model compounds: Acetic acid, phenol and hydroxyacetone. Int J Hydrogen Energy 2014;39:18675–87. https://doi.org/10.1016/j.ijhydene.2014.01.142.

[18] Cheng F, Dupont V. Steam reforming of bio-compounds with auto-reduced nickel catalyst. Catalysts 2017;7(12):114.

[19] Montero C, Remiro A, Benito PL, Bilbao J, Gayubo AG. Optimum operating conditions in ethanol steam reforming over a Ni/$La_2O_3$-α$Al_2O_3$ catalyst in a fluidized bed reactor. Fuel Process Technol 2018;169:207–16.

[20] Li X, Zhang Z, Zhang L, Fan H, Li X, Liu Q, et al. Investigation of coking behaviors of model compounds in bio-oil during steam reforming. Fuel 2020;265:116961.

[21] Bizkarra K, Bermudez JM, Arcelus-Arrillaga P, Barrio VL, Cambra JF, Millan M. Nickel based monometallic and bimetallic catalysts for synthetic and real bio-oil steam reforming. Int J Hydrogen Energy 2018;43:11706–18. https://doi.org/10.1016/j.ijhydene.2018.03.049.

[22] Italiano C, Bizkarra K, Barrio VL, Cambra JF, Pino L, Vita A. Renewable hydrogen production via steam reforming of simulated bio-oil over Ni-based catalysts. Int J Hydrogen Energy 2019;44:14671–82. https://doi.org/10.1016/j.ijhydene.2019.04.090.

[23] Megía PJ, Vizcaíno AJ, Ruiz-Abad M, Calles JA, Carrero A. Coke evolution in simulated bio-oil aqueous fraction steam reforming using Co/SBA-15. Catal Today 2021;367:145–52. https://doi.org/10.1016/j.cattod.2020.04.069.

[24] Seyedeyn Azad F, Abedi J, Salehi E, Harding T. Production of hydrogen via steam reforming of bio-oil over Ni-based catalysts: Effect of support. Chem Eng J 2012;180:145–50. https://doi.org/10.1016/j.cej.2011.11.027.

[25] Wu C, Dong L, Huang J, Williams PT. Optimising the sustainability of crude bio-oil via reforming to hydrogen and valuable by-product carbon nanotubes. RSC Adv 2013;3:19239–42. https://doi.org/10.1039/c3ra43828g.

[26] Remiro A, Valle B, Aguayo AT, Bilbao J, Gayubo AG. Steam reforming of raw bio-oil in a fluidized bed reactor with prior separation of pyrolytic lignin. Energy Fuels 2013;27:7549–59. https://doi.org/10.1021/ef401835s.

[27] Valle B, Aramburu B, Benito PL, Bilbao J, Gayubo AG. Biomass to hydrogen-rich gas via steam reforming of raw bio-oil over Ni/$La_2O_3$-α$Al_2O_3$ catalyst: Effect of space-time and steam-to-carbon ratio. Fuel 2018;216:445–55.

[28] Remón J, Broust F, Volle G, García L, Arauzo J. Hydrogen production from pine and poplar bio-oils by catalytic steam reforming. Influence of the bio-oil composition on the process. Int J Hydrogen Energy 2015;40:5593–608. https://doi.org/10.1016/j.ijhydene.2015.02.117.

[29] Gao N, Han Y, Quan C, Wu C. Promoting hydrogen-rich syngas production from catalytic reforming of biomass pyrolysis oil on nanosized nickel-ceramic catalysts. Appl Therm Eng 2017;125:297–305. https://doi.org/10.1016/j.applthermaleng.2017.07.028.

[30] Remiro A, Arandia A, Oar-Arteta L, Bilbao J, Gayubo AG. Regeneration of $NiAl_2O_4$ spinel type catalysts used in the reforming of raw bio-oil. Appl Catal B Environ 2018;237:353–65. https://doi.org/10.1016/j.apcatb.2018.06.005.

[31] García-Gómez N, Valecillos J, Remiro A, Valle B, Bilbao J, Gayubo AG. Effect of reaction conditions on the deactivation by coke of a $NiAl_2O_4$ spinel derived catalyst in the steam reforming of bio-oil. Appl Catal B Environ 2021;297:120445. https://doi.org/10.1016/j.apcatb.2021.120445.

[32] Pinheiro Pires AP, Arauzo J, Fonts I, Domine ME, Fernández Arroyo A, Garcia-Perez ME, et al. Challenges and opportunities for bio-oil refining: A review. Energy Fuels 2019;33(6):4683–720.

[33] Gholizadeh M, Hu X, Liu Q. A mini review of the specialties of the bio-oils produced from pyrolysis of 20 different biomasses. Renew Sustain Energy Rev 2019;114:109313.

[34] García-Gómez N, Valle B, Valecillos J, Remiro A, Bilbao J, Gayubo AG. Feasibility of online pre-reforming step with dolomite for improving Ni spinel catalyst stability in the steam reforming of raw bio-oil. Fuel Process Technol 2021;215:106769. https://doi.org/10.1016/j.fuproc.2021.106769.

[35] Remiro A, Valle B, Oar-Arteta L, Aguayo AT, Bilbao J, Gayubo AG. Hydrogen production by steam reforming of bio-oil/bio-ethanol mixtures in a continuous thermal-catalytic process. Int J Hydrogen Energy 2014;39:6889–98. https://doi.org/10.1016/j.ijhydene.2014.02.137.

[36] Valecillos J, Iglesias-Vázquez S, Landa L, Remiro A, Bilbao J, Gayubo AG. Insights into the reaction routes for $H_2$ formation in the ethanol steam reforming on a catalyst derived from $NiAl_2O_4$ spinel. Energy Fuels 2021;35:17197–211. https://doi.org/10.1021/acs.energyfuels.1c01670.

[37] Remiro A, Arandia A, Bilbao J, Gayubo AG. Comparison of Ni based and Rh based catalyst performance in the oxidative steam reforming of raw bio-oil. Energy Fuels 2017;31:7147–56. https://doi.org/10.1021/acs.energyfuels.7b00735.

[38] He L, Hu S, Jiang L, Syed-Hassan SSA, Wang Y, Xu K, et al. Opposite effects of self-growth amorphous carbon and carbon nanotubes on the reforming of toluene with Ni/a-$Al_2O_3$ for hydrogen production. Int J Hydrogen Energy 2017;42:14439–48. https://doi.org/10.1016/j.ijhydene.2017.04.230.

[39] Arandia A, Remiro A, Valle B, Bilbao J, Gayubo AG. Deactivation of Ni spinel derived catalyst during the oxidative steam reforming of raw bio-oil. Fuel 2020;276:117995. https://doi.org/10.1016/j.fuel.2020.117995.

[40] Ochoa A, Valle B, Resasco DE, Bilbao J, Gayubo AG, Castaño P. Temperature programmed oxidation coupled with in situ techniques reveal the nature and location of coke deposited on a Ni/$La_2O_3$-α$Al_2O_3$ catalyst in the steam reforming of bio-oil. ChemCatChem 2018;10:2311–21. https://doi.org/10.1002/cctc.201701942.

[41] Hu S, He L, Wang Yi, Su S, Jiang L, Chen Q, et al. Effects of oxygen species from Fe addition on promoting steam reforming of toluene over Fe–Ni/$Al_2O_3$ catalysts. Int J Hydrogen Energy 2016;41(40):17967–75.

[42] He L, Hu S, Jiang L, Liao G, Zhang L, Han H, et al. Co-production of hydrogen and carbon nanotubes from the decomposition/reforming of biomass-derived organics over Ni/α-$Al_2O_3$ catalyst: Performance of different compounds. Fuel 2017;210:307–14.

[43] He L, Liao G, Hu S, Jiang L, Han H, Li H, et al. Effect of temperature on multiple competitive processes for co-production of carbon nanotubes and hydrogen during catalytic reforming of toluene. Fuel 2020;264:116749.

[44] Acomb JC, Wu C, Williams PT. Effect of growth temperature and feedstock:catalyst ratio on the production of carbon nanotubes and hydrogen from the pyrolysis of waste plastics. J Anal Appl Pyrolysis 2015;113:231–8. https://doi.org/10.1016/j.jaap.2015.01.012.

[45] Vicente J, Ereña J, Montero C, Azkoiti MJ, Bilbao J, Gayubo AG. Reaction pathway for ethanol steam reforming on a Ni/$SiO_2$ catalyst including coke formation. Int J Hydrogen Energy 2014;39(33):18820–34.

[46] Montero C, Remiro A, Valle B, Oar-Arteta L, Bilbao J, Gayubo AG. Origin and nature of coke in ethanol steam reforming and its role in deactivation of Ni/$La_2O_3$-α$Al_2O_3$ catalyst. Ind Eng Chem Res 2019;58:14736–51. https://doi.org/10.1021/acs.iecr.9b02880.

[47] Ochoa A, Bilbao J, Gayubo AG, Castaño P. Coke formation and deactivation during catalytic reforming of biomass and waste pyrolysis products: A review. Renew Sustain Energy Rev 2020;119:109600. https://doi.org/10.1016/j.rser.2019.109600.

[48] Zhang Z, Hu X, Zhang L, Yang Y, Li Q, Fan H, et al. Steam reforming of guaiacol over Ni/$Al_2O_3$ and Ni/SBA-15: Impacts of support on catalytic behaviors of nickel and properties of coke. Fuel Process Technol 2019;191:138–51.

[49] Zhang Z, Sun Y, Wang Y, Sun K, Gao Z, Xu Q, et al. Steam reforming of acetic acid and guaiacol over Ni/Attapulgite catalyst: Tailoring pore structure of the catalyst with KOH activation for enhancing the resistivity towards coking. Mol Catal 2020;493:111051.

[50] Sing KSW, Everett DH, Haul RAW, Moscou L, Pierotti RA, Rouquerol J, et al. Reporting physisorption data for Gas/Solid systems with special reference to the determination of surface area and porosity. Pure Appl Chem 1985;57:603–19. https://doi.org/10.1351/pac198557040603.

[51] Montero C, Ochoa A, Castaño P, Bilbao J, Gayubo AG. Monitoring $Ni^0$ and coke evolution during the deactivation of a Ni/$La_2O_3$-α$Al_2O_3$ catalyst in ethanol steam reforming in a fluidized bed. J Catal 2015;331:181–92. https://doi.org/10.1016/j.jcat.2015.08.005.

[52] Guil-Lopez R, Navarro RM, Ismail AA, Al-Sayari SA, Fierro JLG. Influence of Ni environment on the reactivity of Ni-Mg-Al catalysts for the acetone steam reforming reaction. Int J Hydrogen Energy 2015;40:5289–96. https://doi.org/10.1016/j.ijhydene.2015.01.159.

[53] Yang X, Weng Y, Li M, Sun B, Li Y, Wang Y. Enhanced hydrogen production by steam reforming of acetic acid over a Ni catalyst supported on mesoporous MgO. Energy Fuels 2016;30:2198–203. https://doi.org/10.1021/acs.energyfuels.5b02615.

[54] Venkataraman A, Amadi EV, Chen Y, Papadopoulos C. Carbon nanotube assembly and integration for applications. Nanoscale Res Lett 2019;14:220. https://doi.org/10.1186/s11671-019-3046-3.

[55] Mueanngern Y, Li C-H, Spelic M, Graham J, Pimental N, Khalifa Y, et al. Deactivation-free ethanol steam reforming at nickel-tipped carbon filaments. Phys Chem Chem Phys 2021;23(20):11764–73.
[56] Ferrari A, Robertson J. Interpretation of Raman spectra of disordered and amorphous carbon. Phys Rev B - Condens Matter Mater Phys 2000;61:14095–107. https://doi.org/10.1103/PhysRevB.61.14095.
[57] Li J, Jia P, Hu X, Dong D, Gao G, Geng D, et al. Steam reforming of carboxylic acids for hydrogen generation: Effects of aliphatic chain of the acids on their reaction behaviors. Mol Catal 2018;450:1–13.
[58] Bokobza L, Bruneel JL, Couzi M. Raman spectroscopic investigation of carbon-based materials and their composites. Comparison between carbon nanotubes and carbon black. Chem Phys Lett 2013;590:153–9. https://doi.org/10.1016/j.cplett.2013.10.071.
[59] Choi YC, Min K-I, Jeong MS. Novel method of evaluating the purity of multiwall carbon nanotubes using raman spectroscopy. J Nanomater 2013;2013:1–6.
[60] Jorio A, Saito R. Raman spectroscopy for carbon nanotube applications. J Appl Phys 2021;129(2):021102.
[61] Schuepfer DB, Badaczewski F, Guerra-Castro JM, Hofmann DM, Heiliger C, Smarsly B, et al. Assessing the structural properties of graphitic and non-graphitic carbons by Raman spectroscopy. Carbon 2020;161:359–72.
[62] Ochoa A, Aramburu B, Valle B, Resasco DE, Bilbao J, Gayubo AG, et al. Role of oxygenates and effect of operating conditions in the deactivation of a Ni supported catalyst during the steam reforming of bio-oil. Green Chem 2017;19(18):4315–33.
[63] Gayubo AG, Vicente J, Ereña J, Montero C, Olazar M, Bilbao J. Comparison of Ni and Co catalysts for ethanol steam reforming in a fluidized bed reactor. Catal Letters 2014;144(7):1134–43.
[64] Koo KY, Lee SH, Jung UH, Roh HS, Yoon WL. Syngas production via combined steam and carbon dioxide reforming of methane over Ni-Ce/$MgAl_2O_4$ catalysts with enhanced coke resistance. Fuel Process Technol 2014;119:151–7. https://doi.org/10.1016/j.fuproc.2013.11.005.
[65] Hu X, Zhang L, Lu G. Pruning of the surface species on Ni/$Al_2O_3$ catalyst to selective production of hydrogen via acetone and acetic acid steam reforming. Appl Catal A Gen 2012;427–428:49–57. https://doi.org/10.1016/j.apcata.2012.03.029.
[66] Van Der Lee MK, Van Dillen AJ, Geus JW, De Jong KP, Bitter JH. Catalytic growth of macroscopic carbon nanofiber bodies with high bulk density and high mechanical strength. Carbon N Y 2006;44:629–37. https://doi.org/10.1016/j.carbon.2005.09.031.
[67] Galetti AE, Gomez MF, Arrúa LA, Abello MC. Hydrogen production by ethanol reforming over NiZnAl catalysts. Influence of Ce addition on carbon deposition. Appl Catal A Gen 2008;348:94–102. https://doi.org/10.1016/j.apcata.2008.06.039.
[68] Kawamoto H, Murayama M, Saka S. Pyrolysis behavior of levoglucosan as an intermediate in cellulose pyrolysis: Polymerization into polysaccharide as a key reaction to carbonized product formation. J Wood Sci 2003;49:469–73. https://doi.org/10.1007/s10086-002-0487-5.